

Kidney Stones and Microfluidics

Effects of Hyaluronic Acid on the kinetics of Calcium Oxalate in Artificial Urine

Manzoor Rashid Alhaji Nuhu

Technische Universiteit Delft



KIDNEY STONES AND MICROFLUIDICS

EFFECTS OF HYALURONIC ACID ON THE KINETICS OF CALCIUM OXALATE IN ARTIFICIAL URINE

by

Manzoor Rashid Alhaji Nuhu

4770374

in partial fulfillment of the requirements for the degree of

Master of Science
in Mechanical Engineering

at the Delft University of Technology,
to be defended publicly on Friday December 11, 2020 at 9:00 AM.

Supervisor:	Dr. H.B. Eral,	TU Delft
	Ir. Fatma Ibis	TU Delft
Thesis committee:	Prof.dr.ir. J.T. Padding,	TU Delft
	Dr. H.B. Eral,	TU Delft
	Dr. Angeliki Laskari,	TU Delft

An electronic version of this thesis is available at <http://repository.tudelft.nl/>.
The front cover picture is a combined image of droplets containing COM and COD under white light and crossed polarized light.

ABSTRACT

Kidney stones may be uncommon in certain parts of the world. On the other hand, considering the percentage of cases in the western world, one can say it is worrisome. Anyone can have kidney stones, which may be easily passed out of the kidney through the urine. It only becomes a cause for concern when the stones grow beyond a certain size. They can cause flank and abdominal pains, fever, painful urination, etc., and can subsequently result in kidney failure if the patient has only one kidney present. In that case, a kidney stone patient may require the attention of a nephrologist. Advancement in technology has provided conventional techniques such as ureteroscopy (URS), percutaneous nephrolithotomy (PNL) and shockwave lithotripsy (SWL) for treating kidney stones.

One may wonder what exactly these stones are. They are nothing extraordinary but rather made of calcium oxalate (CaOx) crystals which are formed from a supersaturated urine. CaOx crystal which is a product of crystallization occurs in two forms, calcium oxalate monohydrate (COM) and calcium oxalate dihydrate (COD). Crystallization is a very simple and effective purification and phase separation process used in the chemical and pharmaceutical industry. This process is usually influenced by many factors such as concentration, temperature, mixing, impurities, etc.

The presence of oxalate in urine is a major contributor to the formation of kidney stones. High concentration of oxalate combines with calcium to form CaOx. On the other hand, injury to the kidney tubular epithelial cells results in the expression of Hyaluronic acid (HA). HA has since been considered as a binding agent which causes the retention of kidney stones. Furthermore, some scientists are of the idea that HA may also influence the formation of kidney stones.

A novel method was developed to study the nucleation kinetics of CaOx in artificial urine under the influence of varying oxalate and HA concentrations. The method involved crystallizing CaOx (COM, COD) in emulsions (micro-droplets) that were generated by and stored in a microfluidic device. Incorporating polarized light microscopy also allowed COM and COD to be detected at the same time. The cumulative probability distribution as a function of induction time for COM and COD was determined and fitted to the Weibull model. The induction time is the average time at which the first crystal is detected in the droplets.

As was expected, higher oxalate concentration shortened the induction time for both COM and COD. Surprisingly, increasing HA concentration induced the formation of COM while inhibiting the formation of COD. In general, the frequency of COD was always less than that of COM. In conclusion, the idea that HA played a role in the formation of kidney stones was confirmed. This was the most important part of the research.

Keywords: Kidney stones, URS, PNL, SWL, Nucleation, Emulsions, Polarized light microscopy, Weibull model.

ACKNOWLEDGEMENTS

I begin by thanking Dr. H.B. Eral for being an amazing supervisor. Thank you for all the support and for making things look easy while in fact they weren't. I have always admired you and I am proud to have worked under your supervision. Your lectures were so outstanding that I never wanted to miss a class. Before I forget, thank you for the internship opportunity in Japan.

This work would not have been possible without my daily supervisor ir. Fatma Ibis. I am proud of the work we have achieved together and most importantly during the Covid-19 lockdown. I woke up everyday knowing that you will be at the laboratory even though it was highly risky healthwise. That was some next level determination and it will definitely go down in our history books.

I also thank Dr.ir. H.J.M. Kramer and Prof. dr. A. E. D. M. van der Heijden for their incredible suggestions and encouragements during the weekly meetings. Hearing the phrase "nice work" from them really motivated me to give my very best.

Dr. ir. Frederico Marques Penha, you have been so amazing throughout my thesis work and I am grateful for all your support. Although, I did break a couple of the laboratory rules, you were there to keep me in check for the safety of everyone. I am proud to call you a friend and truly, you will always have a place in my heart. Ir. Tsun Wang Yu, thank you for the solid experimental basis you developed. The accomplishment of this work wouldn't have been possible without your work.

Last but not the least, I would like to thank Prof.dr.ir. J.T. Padding and Dr. Angeliki Laskari for taking time to be part of my thesis defense.

Lastly, I would like to thank my family for all the support and I should say I love you so much. I dedicate this work to them and most especially my dad (may he rest in peace), as he has been the main source of inspiration for me.

*Manzoor Rashid Alhaji Nuhu
Delft, December 2020*

CONTENTS

Abstract	iii
Acknowledgements	v
List of Figures	ix
List of Tables	xi
List of Symbols	xiii
Abbreviations	xv
1 Introduction	1
1.1 Urolithiasis or Kidney Stone Disease	1
1.1.1 Types of Kidney Stones	2
1.1.2 Treatment	3
1.2 A Review of Hyaluronic Acid (HA)	3
1.3 Artificial Urine (AU)	4
1.4 Research Goals and Objectives	5
2 Crystallization	7
2.1 Theoretical background	7
2.1.1 Crystalline State	7
2.1.2 Supersaturation	8
2.1.3 Nucleation	9
2.1.4 Primary Nucleation	9
2.1.5 Induction Time and Models	12
3 Raman	15
3.1 Raman Spectroscopy	15
3.1.1 Quantitative Approach	15
3.2 Materials and Methods	17
3.3 Preparation procedure of samples for Raman analysis	18
3.3.1 Preparation of Artificial Urine	18
3.3.2 COM (supplier)	18
3.3.3 <i>CaOx</i> ([Ca]=4.3mM, [Ox]=4.3mM)	18
3.3.4 <i>CaOx</i> ([Ca]=6.0mM, [Ox]=1.2mM)	19
3.3.5 Artificial urine filtrate from COM (supplier) solution	19
3.3.6 Artificial urine filtrate from <i>CaOx</i> solution	19
3.4 Results	19
3.5 Discussions	21
4 Polarized Light microscopy	23
4.1 Birefringence of Calcium Oxalate Crystal under Polarized Light	23
4.1.1 Crossed Polarization	24
5 Production of droplet-based microfluidic device	27
5.1 Materials and Methods	27
5.1.1 Hydrophobization	28
5.1.2 Polydimethylsiloxane (PDMS) Molding	28
5.1.3 Spin coating	28
5.1.4 Semicuring and Bonding	28
5.2 Results and Discussions	29

6	Microfluidic crystallization	33
6.1	Experimental setup and procedure	33
6.2	Materials and Methods	35
6.2.1	Preparation of Dispersed Phase at Different Oxalate Concentration	35
6.2.2	Preparation of Dispersed Phase at Different HA Concentrations	36
6.2.3	Preparation of Continuous Phase	36
6.2.4	Microfluidic Chip Injection	36
6.2.5	Polarized Light Microscopy	36
6.2.6	Induction Time Measurement	37
6.3	Results and Discussions	39
6.3.1	Induction Time of Calcium Oxalate at Different Oxalate Concentrations	39
6.3.2	Induction Time of Calcium Oxalate at Different HA Levels	44
7	Conclusions & Recommendations	49
7.1	Conclusions	49
7.1.1	Raman Spectroscopy	49
7.1.2	Polarized Light Microscopy	49
7.1.3	Induction Time Measurements	49
7.2	Recommendations	51
	Appendices	53
A	MATLAB code for plotting data from Raman experiments	55
B	Python code for τ & k calculation	57
	Bibliography	61

LIST OF FIGURES

1.1	Location of kidney stones in the upper tract of the urinary system [1]	2
1.2	Type of stones. (A) cystine crystal; (B) struvite crystals; (C) calcium oxalate dihydrate crystals; (D) calcium oxalate monohydrate crystal; (E) rectangular uric acid crystals; and (F) rhomboidal uric acid crystals [2]	2
2.1	Crystallographic axes for describing monoclinic and tetragonal system [3]	7
2.2	Simple forms of tetragonal and monoclinic systems [4], Refer to figure 3.8 and 3.9 for crystal image	8
2.3	A schematic representation of solubility diagram [5]	8
2.4	Free energy diagram explaining the concept of critical radius and energy [3]	10
2.5	Comparison between ΔG_{crit} (i.e., ΔG^*) for homogeneous and heterogeneous nucleation [6]	11
2.6	A schematic representation for heterogeneous nucleation.	12
2.7	Experimentally determined probability distributions $P(t)$ of induction times. Dotted lines are fits to Eq 2.30	14
3.1	The energy transition process in Stokes (left) and Anti-Stokes (right) Raman scattering. The (i) denotes initial energy state, whereas (f) denotes the final energy state.	16
3.2	A representation of Rayleigh and Raman spectra showing the positive and negative values of [7]	16
3.3	Raman Rxn2 analyzer with phase-optimized sampling probe	17
3.4	Raman spectra of artificial urine filtrates	19
3.5	Raman spectra showing significant spectral difference which allows COM (supplier) and CaOx peaks to be distinguished from any background noise (i.e. artificial urine-AU)	20
3.6	Raman spectra for COM and CaOx peaks within $380\text{-}1100\text{ cm}^{-1}$ region	21
3.7	Raman spectra for COM and COD peaks within $1100\text{-}1800\text{ cm}^{-1}$ region	21
3.8	The polymorphic forms of calcium oxalate crystals in artificial urine obtained under non-equimolar conditions of $[\text{CaCl}_2] = 6.0\text{mM}$ and $[\text{NaOx}] = 1.2\text{mM}$.	22
3.9	The polymorphic forms of calcium oxalate crystals in artificial urine obtained under equimolar conditions of $[\text{CaCl}_2] = 4.3\text{mM}$ and $[\text{NaOx}] = 4.3\text{mM}$.	22
4.1	Birefringent crystal between crossed polarizers [8]	23
4.2	Schematic representation of crossed polarization	24
4.3	Orientation of a birefringent crystal under crossed polarized light with its optical axis aligned parallel to the transmission azimuth of the polarizer [8]	24
4.4	Polymorphic forms of calcium oxalate in a microfluidic droplet as seen under (a) white light and (b) crossed polarized light, using 20x objective lens and a polarizer angle of 0° .	25
4.5	Orientation of a birefringent crystal under crossed polarized light with its optical axis aligned at angle to the transmission azimuth of the polarizer [8]	25
5.1	PDMS on a glass slide in a spincoater.	28
5.2	PDMS-glass slide bonding process.	29
5.3	Droplet-based 3D printed mold designed by Tsun [9].	29
5.4	Microscope image of device showing droplet formation, internal mixing, and storage. Scale bar = $100\mu\text{m}$	30
5.5	Dimensions of a microfluidic droplet. width = $396.60\mu\text{m}$ and length = $850.86\mu\text{m}$	30
5.6	A complete droplet-based microfluidic device highlighting the channels, three inlets, and one outlet port.	31
6.1	Microfluidic crystallization experiment setup for induction time measurements.	34

6.2	Time lapse images of COM and COD (at [Ca]=6.0mM, [Ox]=1.2mM) using polarized light microscopy	37
6.3	Image of a droplet highlighting COM (white) and COD (black) with the use of polarized light microscopy at time t=240min, polarizer angle = 20°, and scale bar = 100μm	38
6.4	A large image of the microfluidic device as per the specified area (17×12) using 10x objective lens	38
6.5	Image of droplets containing COM only or COM and COD	39
6.6	Individual probability curves of COM vs COD at different oxalate concentrations	40
6.7	Combined probability curves for COM at different oxalate concentrations	41
6.8	Combined probability curves for COD at different oxalate concentrations	42
6.9	Effect of COD on COM induction time at different oxalate concentration	43
6.10	Individual probability curves of COM vs COD at different HA concentrations	44
6.11	Combined probability curves for COM at different HA concentrations	45
6.12	Combined probability curves for COD at different HA concentrations	46
6.13	Effect of COD on COM detection time at different HA concentrations	47

LIST OF TABLES

1.1	Composition of artificial urine used in this research according to Streit et al [10]	5
3.1	Equipment used for Raman spectroscopy experiments	18
3.2	Amount of chemicals used for preparation of artificial urine (AU)	18
3.3	Amount of chemicals required to prepare samples in AU for Raman spectroscopy experiments	18
3.4	Comparison of between thesis study and literature Raman bands	20
5.1	Chemicals and materials used in making droplet-based microfluidic device.	27
5.2	Equipment used in making droplet-based microfluidic device.	27
6.1	Equipment used during microfluidic crystallization experiments.	35
6.2	Chemicals needed for microfluidic crystallization experiments	35
6.3	Amount chemicals required to prepare the dispersed phase	35
6.4	Amount chemical required to prepare dispersed phase at different HA levels	36
6.5	τ and k parameters for COM obtained from the fitted Weibull model at different oxalate concentration	42
6.6	Median nucleation time and nucleation rate of COM at different oxalate concentration	42
6.7	τ and k parameters for COD obtained from the fitted Weibull model at different oxalate concentration	43
6.8	Median nucleation time and nucleation rate of COD at different oxalate concentration	43
6.9	τ and k parameters for COM obtained from the fitted Weibull model at different HA concentration	45
6.10	Median nucleation time and nucleation rate of COM at different HA concentration	45
6.11	τ and k parameters for COD obtained from the fitted Weibull model at different HA concentrations	46
6.12	Median nucleation time and nucleation rate of COD at different HA concentration	46

LIST OF SYMBOLS

dG	Small change in free energy	J
dn	Small change in mole number of a species	mol
$\Delta\mu$	Chemical potential	J/mol
μ_s	Chemical potential of solute in solution	J/mol
μ_p	Chemical potential of solute as precipitate	J/mol
R	Universal gas constant	$\text{J mol}^{-1} \text{K}^{-1}$
a	Solution activity of solute	mol L^{-1}
a_o	Solution activity of solute after precipitation at equilibrium	mol L^{-1}
C	Molar concentration of solute before equilibrium	mol L^{-1}
C_o	Molar concentration of solute at equilibrium	mol L^{-1}
γ	Activity coefficient	-
S	Supersaturation ratio	-
α	Cluster volume shape factor	-
β	Cluster area shape factor	-
L	Cluster length	m
ΔG	Gibbs excess free energy	J
ΔG_S	Surface Gibbs free energy	J
ΔG_V	Volume Gibbs free energy	J
ΔG_v	Gibbs free energy per unit volume	J/m^3
ΔG_{crit}	Critical Gibbs excess free energy	J
ΔG_{c^*}	Critical Gibbs excess free energy	J
γ	Interfacial tension	N/m
r_c	Cluster radius	m
r_c	Cluster critical radius	m
J	Nucleation rate	$\text{nuclei/m}^3\text{s}$
k_B	Boltzmann constant	$\text{m}^2 \text{kg s}^{-2} \text{K}^{-1}$
v	Molecular volume of crystal	m^3
A	Pre-exponential kinetic parameter	$\text{m}^3 \text{s}^{-1}$
B	Exponential thermodynamic parameter	-
γ_{eff}	Effective interfacial tension	N/m
γ_{ps}	Interfacial tension between supersaturated solution and heterogeneous particle	N/m
γ_{pn}	Interfacial tension between nucleus and heterogeneous particle	N/m
W^*	Crystal nucleation work	J
c	Shape factor	-
Z	Zeldovich factor	-
f^*	Attachment frequency	s^{-1}
C_0	Concentration of nucleation sites	Nuclei/m^{-3}
α	Crystal volume fraction	-
G	Linear growth rate	m/s
P_m	Probability of finding m nuclei	-
N	Average number of nuclei formed within a specific time frame	-
P_o	Probability of finding no nuclei	-
V	Volume of a droplet	m^3
τ	Mean Induction time	s
t_j	Specific time interval	s
t	Overall detection time	s

t_{MED}	Median nucleation time	s
T	Absolute temperature	K
k	Shape parameter	-
$P(t)$	Probability of forming nuclei at time t	-
$M^+(t)$	Number droplets containing detectable crystals at time t	-
M	Total number of droplets	-

ABBREVIATIONS

MSMPR	Mixed-Suspension Mixed-Product Removal
GAGs	Glycosaminoglycans
AU	Artificial Urine
HA	Hyaluronic Acid
URS	Ureteroscopy
PNL	Percutaneous Nephrolithotomy
SWL	Shockwave Lithotripsy
RSFs	Stone-Free Rates
CaOx	Calcium Oxalate
COM	Calcium Oxalate Monohydrate
COD	Calcium Oxalate Dihydrate
COT	Calcium Oxalate Trihydrate
AFM	Atomic Force Microscopy
CNT	Classical Nucleation Theory
AiO	All-in-One
SS	Supersaturation

1

INTRODUCTION

Crystallization is basically a purification and a phase separation process which is used in the pharmaceutical and chemical industries for production of chemicals such as fertilizers and other high-valued products. Not only is it an industrial process but also a biological process occurring right within the human body.

Kidney stone is a product of crystallization that consist of aggregates of tiny crystals. Large stones can be problematic when an individual passes urine for instance. Developing drugs to combat such a condition can be time consuming and less efficient with the mainstream technologies. Also, current development of drugs is very costly. Clinical trials are less effective as individuals react differently to drugs. Babies, for example are at risk as clinical trials are not done on them. The inefficiency of drug development and clinical trials has led to a new branch of techno-medicine where a home for cells outside of the body (organ/human on chip) is developed to provide the basic functionality of human organ(s). Drug development and clinical trials can then be personalized by putting, for example, one's own stem cells in the chip and learning how they interact with the drugs.

In this work, only the chip is considered which is the first stage of to achieving an organ on a chip system. In vitro kidney stone research that involves crystallization of CaOx needs to be done in artificial urine so as to mimic the renal environment as much as possible. Several studies on this subject have made use of artificial urine and MSMPR crystallizers. However, these crystallizers may perhaps, provide a system (fluctuating temperature and macromixing) which is on a larger scale compared to the kidney. Therefore, an artificial urine (AU) environment was incorporated within a microfluidic device, also referred to as microfluidic chip.

1.1. UROLITHIASIS OR KIDNEY STONE DISEASE

Understanding the epidemiology of kidney stone is very important to providing underlying methods to combat it. The occurrence of kidney stones varies depending on geography, age, sex, and even race. The presence of kidney stones among people all over the world is reported to be around 12%, while 5-10% of western world is reported to be living with kidney stones as well [11, 12]. Most surveys carried out also indicate a higher percentage of kidney stone occurrence and reoccurrence in males (10-12%) compared to females (5-6%) between ages of 20-49 years [13].

Certain abnormalities and high levels of chemical composition in urine creates a perfect stage for the occurrence of kidney stones. Several reports suggests that there is also a link between dietary conditions and kidney stone formation. High intake of dietary calcium, oxalate, salts, and animal protein may all increase the risk of stone formation [14, 15]. However, lowering the intake of dietary calcium alone is no longer recommended for preventing reoccurring kidney stones, specifically calcium stones [16].

Kidney stones are formed in different parts of the urinary system such as the kidney, ureter, urethra, and urinary bladder. In line with most research, most stones are found in the upper urinary tract which consist of the ureter and the kidneys [17]. The kidneys in particular are the filters of the human body. They filter out waste product and excess water from the blood and eliminate them as urine. The ureter on the other hand,

serves as the connecting tube between the kidney and the bladder. They are responsible for draining out urine from the kidneys into the bladder. During filtration, supersaturation with respect to certain compounds is created thereby leading the potential formation of kidney stones. The presence of these stones in the kidney calyces are considered harmless. The problem arises when the stones get stuck in the ureter.

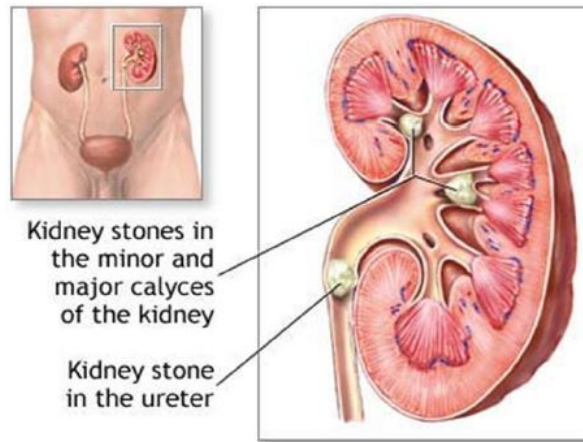


Figure 1.1: Location of kidney stones in the upper tract of the urinary system [1]

Every single human is capable of forming these stones, but the stone has to grow to a certain size (above 7 mm) for patients to require medical attention [18]. Because of the different locations of stones in the urinary system, signs and symptoms may differ in many ways. Some general signs and symptoms include the following.

- Blood in urine
- Flank and abdominal pains
- Urinary obstruction and retention
- Painful urination
- Fever, nausea and vomiting

1.1.1. TYPES OF KIDNEY STONES

Kidney stones have been known to man for ages and extensive research been carried to explain the causes and mechanisms for its formation. Kidney stones come in different types with some having a higher frequency than others. The stones are categorized based on the composition of stone-forming substance. In essence, there are 4 different types of kidney stones 1) Calcium, 2) Struvite, 3) Uric acid, and 4) Cystine stones.

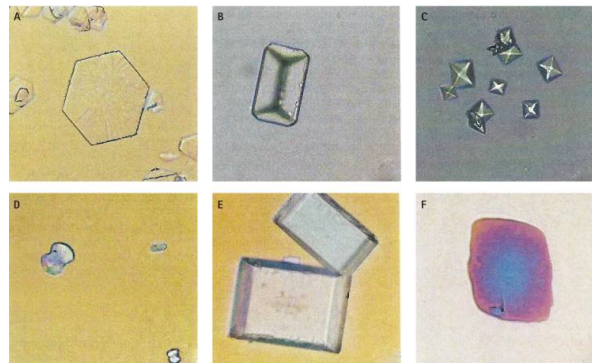


Figure 1.2: Type of stones. (A) cystine crystal; (B) struvite crystals; (C) calcium oxalate dihydrate crystals; (D) calcium oxalate monohydrate crystal; (E) rectangular uric acid crystals; and (F) rhomboidal uric acid crystals [2]

CALCIUM STONES

Statistics show that 70-80% of kidney stones contain calcium oxalate and calcium phosphate (Brushite), with calcium oxalate (CaOx) being the principal component [2, 19, 20]. Only 5% of kidney stones is made up of calcium phosphate which occurs when the urine pH is high (pH > 7.5). In contrast, an acidic urine, (pH 5.0-6.5) rather favours the formation of calcium oxalate. The most common type of CaOx which has the greatest propensity of forming stones is the thermodynamically stable COM followed by the less stable COD [21, 22]. COM crystals are considered pathogenic due to their usual presence in the urine of stone formers, whereas COD is physiological as they can be found in the urine of healthy individuals when it is concentrated [21]. Although there is a third type of CaOx which is the unstable COT, however, its presence in kidney stones is rare.

STRUVITE STONES

Struvite is another stone type that is formed due to an infection in the urinary tract. It is made up of magnesium, waste ammonium, and phosphate. The frequency of struvite stones is known to be about 10-15%.

URIC ACID STONES

Not only does excess amount of uric acid in the blood cause gout, it is also a contributor to kidney stone disease. About 3-10% of kidney stones are due to uric acid.

CYSTINE STONES

Cystine is a compound that is considered as a building block for muscles, nerves, etc in the human body. An excess build up of this compound is as a result of a disorder known as cystinuria which leads to the formation of stones. The presence of cystine stone generally accounts for less than 2% of kidney stone cases.

1.1.2. TREATMENT

Advancement in technology has provided useful techniques for the treatment of kidney stones. Some of which include ureteroscopy (URS), percutaneous nephrolithotomy (PNL), and shockwave lithotripsy (SWL). URS is a process where a small telescope is passed through the urethra and the bladder and up through the ureter to the stone location. PNL is done by inserting a nephroscope through an incision on the back of the patient near the pelvis region to get rid of the stones. SWL as the name implies is where shock waves outside the patient's body are directed towards the kidney stones causing them to disintegrate.

The type of treatment technique used is dependent on several factors including on stone size, composition, location, and obesity. SWL for instance is not recommended for cases where patients are obese. Stones made of cystine are very hard and cannot be treated with SWL [2]. However, high stone-free rates (RSFs) are obtained when SWL is used on stones with sizes less than 20 mm. Larger stones (> 20mm) are mostly treated with PNL as it is size independent. Flexible URS may also be used as a second option to PNL for treatment larger stones but SFRs are lower [23].

As mentioned before, the major portion of the kidney stones matrix is made up of crystals. However, there are other organic macromolecules such as glycosaminoglycans (GAGs) which are present within the stone matrix. An example of such molecule is hyaluronic acid.

1.2. A REVIEW OF HYALURONIC ACID (HA)

The process of kidney stone formation is complex and it involves nucleation, growth, and aggregation of crystals [24–26]. Also, adherence of CaOx crystals to tubular surfaces is considered crucial in kidney stone formation [27, 28]. These processes are in one way or the other influenced by an environment containing supersaturated-crystal forming ions (e.g. Mg^+ , Ca^{2+}) and other organic macromolecules such as HA [22].

Hyaluronic acid is basically a high-molecular mass polysaccharide which is identified as a major crystal-binding molecule. The anionic nature of HA allows for complex interaction with cations and Ca^{2+} in particular. It is known to have a promoter and inhibitor effects on nucleation and growth rate respectively [28]. Furthermore, the attachment of crystals in the tubules is considered to be a result of regenerating cells that

expresses HA at their surfaces [27, 29, 30].

The adsorptive nature of COM also allows them to bind to these macromolecules or vice versa, and further for attaching epithelial cells surfaces. During attachment, the residence time is increased allowing sufficient crystal growth and aggregation for problematic stone size [29, 31].

A couple of researches have investigated the mechanisms governing the relationship between HA and COM crystal in different solutions. Other experimental environments such as rat kidney and human renal tubular cells have been used to study the adhesion effect.

Lamontagne [31] demonstrated the adhesion capability between HA and COM crystal and the implication of crystal faces, pH, and citrate. HA-coated AFM probe was brought into contact with the surface of the [100] face COM crystal (15 μ m), in the presence of artificial urine, calcium oxalate solution, and pure water, and immediately retracted. The adhesion work it took to separate HA-probe and crystal surface was then measured.

Artificial urine with increasing pH led to a 25% decrease in energy required to detach HA-probe and crystals surface. The introduction of citrate at varied artificial urine pH led to an overall reduction of interaction forces of molecules. The effect of citrate on adhesion work was very significant, thereby overcoming the influence of pH. The adhesion in calcium oxalate solution was relatively low due to low Ca²⁺ concentration in solution, whereas, no attraction existed in the case of pure water as crystal surfaces became unstable due to dissolution.

Asselman [32] also investigated the role of HA, Osteopontin, and CD-44 in CaOx crystal retention in damaged tubular epithelial cells caused by ethylene glycol in rat kidney. CaOx crystals formed were retained in tubules in the case of injured tubular epithelial cells. Crystal retention however, reduced in the absence of injury. Verhulst [29] showed that crystal binding had reduced when tubular cells in the human nephron expressing HA were digested by an enzyme. The bottom line is that the over expression of HA during cell injury and regeneration may indeed have a role to play in kidney stone formation.

The focus of this research work is to determine the effect of hyaluronic acid on the nucleation kinetics of calcium oxalate monohydrate and calcium oxalate dihydrate. Hyaluronic acid was chosen as an inhibitor and promoter because of the suspicion that it may actually be involved in the nucleation of calcium oxalate.

1.3. ARTIFICIAL URINE (AU)

Urine contains lots of substances capable of influencing the formation of CaOx crystals. Several researches have been done to determine the inhibitor and promoter effect of these substances on crystal formation [33, 34]. An in vitro studies of kidney stones requires environmental conditions similar to human urine. As such, Griffith [35], came up with the first artificial urine which has been altered over the years [36].

Deepak [37], gives a summary of the original and subsequent studies on the constituents of artificial urine used in different research fields. They proposed a composite artificial urine media concentration based on the average values in reference studies. Arndt [36], also made use of artificial composition based on the work of Griffith et al., where a range of equivalent compounds in healthy human urine was also presented. Chutipongtanate [38], analyzed six different artificial urine samples whose compounds were mostly found to be beyond the physiological ranges as seen in normal human urine.

The primary composition of artificial urine used in this research was based on that composed by Streit [10], with a few adjustments to calcium and oxalate levels. These adjustments were done to ensure that concentration levels were within the normal range. This artificial urine amongst many was selected since it provided the solubility data for calcium oxalate.

All human urine are supersaturated with respect to calcium oxalate and, calcium phosphate which mostly depends on pH [39]. This means that once supersaturation is reached, calcium salts will start to crystallize. For this reason, the initial preparation of the artificial urine used in this research contained no calcium and

oxalate. Calcium and oxalate were added later on to obtain a complete artificial urine. Given that this work investigates calcium oxalate precipitates, the amount of calcium used were always within the normal range (i.e. 2.5 – 7.5 mM) [40]. On the other hand, a relatively higher percentage of patients were seen to have hyperoxaluria where oxalate levels were above 0.45 mM [40]. Hence, oxalate levels used in this work always exceeded 0.45 mM.

Table 1.1: Composition of artificial urine used in this research according to Streit et al [10]

Compound	Concentration (mM)	Equivalent compounds in 1L healthy adults human urine [36, 40]	Vendor
NaCl	90	2.5-7.5 mM Calcium	Fluka
KCl	42	1-10 mM magnesium	Emsure
NH ₄ Cl	20	60-200 mM sodium	Sigma-Aldrich
Creatinine	7	20 mM sulphate	Sigma-Aldrich
Urea	300	120-240 mM chloride	Emprove
Tri-sodium citrate	2	20-45 mM phosphate	Emprove
MgSO ₄ · 7H ₂ O	2	30-100 mM potassium	Sigma-Aldrich
Na ₂ SO ₄	13	40 mM ammonium	Sigma-Aldrich
NaH ₂ PO ₄	16	200-600 mM urea	Sigma-Aldrich
CaCl ₂	-	120 mM creatinine	Sigma-Aldrich
Na ₂ C ₂ O ₄	-	-	Sigma-Aldrich
Measured pH	5.57	-	-

¹ CaCl₂ and Na₂C₂O₄ concentrations were not given in this table as the concentrations varied from Raman experiments to microfluidic experiments. It is also important to note that a complete artificial urine includes soluble amounts of CaCl₂ and Na₂C₂O₄ (refer to table [?] and [?]).

1.4. RESEARCH GOALS AND OBJECTIVES

The goal was to determine the induction for COM and COD under varying oxalate and hyaluronic acid concentration. To answer this, certain questions needed to be asked. For example:

- A complex solution such as the AU adopted in this research, what will be the outcome when calcium and oxalate are reacted together ?
- Will the solution appear entirely crystal clear prior to mixing calcium chloride and sodium oxalate ?
- Will the intended crystal be formed or not, and if so which hydrate of the calcium oxalate hydrate is to be expected ?
- How will Hyaluronic acid influence the cumulative probability and induction time of calcium oxalate ?

Answers to these questions will provide certainty for induction time measurements of calcium oxalate in artificial urine.

Prior to this, several trial experiments were done to try and form the basis of the reactants concentration needed. The necessary optimized conditions were required to ensure the formation of individual crystals. It was also important to keep in mind the solubility levels of calcium and oxalate in the chosen artificial urine. Not forgetting the fact that calcium and oxalate levels had to be within normal levels as found in human urine.

To obtain answers to these questions, the experiments were performed in a chronological order as follows.

- Several artificial urine found in the literature were considered. Their compositions were compared with the normal levels in human urine to ensure that the final urine selected had compositions within the normal range.
- Precipitation of COM and COD in artificial urine was done using Crystalline. This was to give a fair idea of the reactant concentrations needed to precipitate.
- Raman spectroscopy was used to monitor the molecular signatures of the crystals formed in 4 ml bulk solution to determine the type of crystals formed.

- Different concentrations of sodium oxalate and hyaluronic acid were used in the microfluidic crystallization part.
- Polarizing light microscopy was used together with droplet-based microfluidics, a new method developed to measure induction time of crystals in micro-droplets. This method provided a means of drawing a clear distinction between the induction time for COM and COD.

2

CRYSTALLIZATION

2.1. THEORETICAL BACKGROUND

At the end of this work, it will be quite nice to be able to interpret and relate the results to CNT. Crystallization basically occurs in two main steps, crystal nucleation and growth. As the aim of this work is focused on nucleation, the theory behind it is very important to the reader. A short introduction of the crystalline state of calcium oxalate is necessary to give the reader a fair idea of the crystal dynamics.

2.1.1. CRYSTALLINE STATE

Aside the existence of some 200 known liquid crystals, solid crystal is what is usually known. They may come in different sizes and external shapes. Crystal shapes are basically defined by the repeating arrangement of molecules, ions, or atoms along the lattice structure of the crystal. Every crystal has several faces which have equal angles to each other (i.e., Haüy's Law of constant interfacial angle), and are symmetric about a point, line, or plane. Based on the symmetry, crystals are classified into seven systems. However, only two of these systems (tetragonal and monoclinic system) define calcium oxalate polymorphs.

COM and COD are polymorphs of calcium oxalate and are chemically identical but have different shapes. COM crystals have a monoclinic system whereas COD crystals have a tetragonal system. Both systems are describes by three axes (x,y,z) and angles (α , β , γ). In the case of a tetragonal system, $\alpha = \beta = \gamma = 90^\circ$ and $x = y \neq z$. In a monoclinic system, $\alpha = \beta = 90^\circ \neq \gamma$ and $x \neq y \neq z$. The shapes of COM and COD observed during experiments are described in the simplest form as seen in figure 2.2.

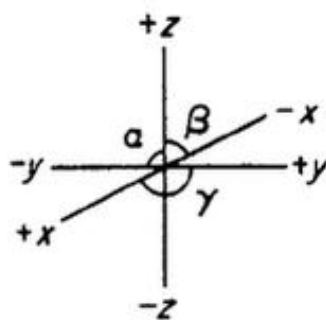


Figure 2.1: Crystallographic axes for describing monoclinic and tetragonal system [3]

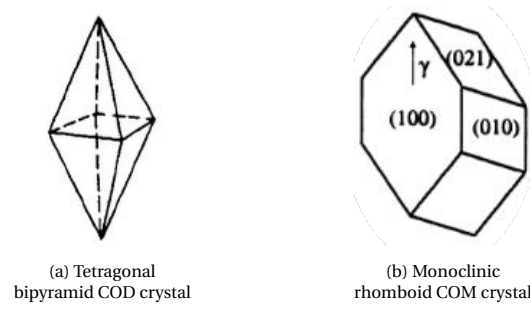


Figure 2.2: Simple forms of tetragonal and monoclinic systems [4], Refer to figure 3.8 and 3.9 for crystal image

2.1.2. SUPERSATURATION

Nucleation mechanism may not be enough to cause crystallization. A certain driving force is also required to drive the solutes into solidification or crystallization. This driving force is known as supersaturation. The schematic representation of supersaturation is often done using the solubility diagram. Solubility plays a major role in crystallization by determining how easily a solute can dissolve in a solvent. In essence, it is defined as the amount of solutes that can dissolve in a certain amount of solvent at a particular constant temperature. A solubility diagram depicts three distinct zone; an undersaturated state where no nucleation occur, a metastable zone where nucleation may occur but not spontaneously, and finally, a supersaturated state where spontaneous nucleation occur. The process of spontaneous nucleation can be achieved either by cooling or evaporation of the saturated solution or by increasing solute concentration.

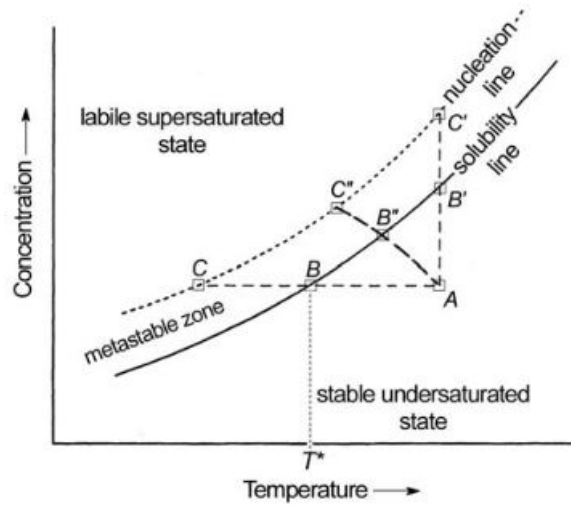


Figure 2.3: A schematic representation of solubility diagram [5]

DEFINING SUPERSATURATION RATIO

The small change in free energy (dG) that is needed to drive a solution to a supersaturated state (i.e., spontaneous nucleation) can be expressed in terms of the chemical potential (μ). The chemical potential of a species can be defined as the energy absorbed or released due a small change in the mole number of the species (dn). Furthermore, the difference, $\Delta\mu$, in the chemical potential of the solute between the solution (μ_s) and the precipitate (μ_p) can be written as

$$\Delta\mu = dG/dn = \mu_s - \mu_p = -RT \ln(a/a_0) \quad (2.1)$$

where R is the universal gas constant, a is the solution activity of the solute before precipitation, and a_0 is the solution activity of the solute when the solution is in equilibrium with the precipitated solute. The activity of any salt or solute may be interpreted as the effective concentration given by

$$a = \gamma C \quad (2.2)$$

The supersaturation ratio is therefore defined as

$$S = \frac{a}{a_o} = \frac{C}{C_o} \quad (2.3)$$

where γ is the activity coefficient and C and C_o are the solute molar concentration before and at equilibrium. At saturation, the solution is basically in equilibrium with the solute, hence, $a = a_o$. Therefore, as indicated in Eq.2.1, there will be no free energy for precipitation.

On the other hand, supersaturation is achieved when $a > a_o$ or when $S > 1$, which is often the case for supersaturated solution. Therefore, there will be free energy for precipitation as depicted in Eq.2.1. In other words, the larger the supersaturation, the more free energy there is for nucleation to occur.

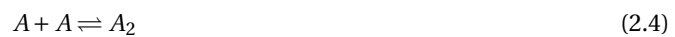
2.1.3. NUCLEATION

The birth of any crystal is as a result of the process called nucleation. Although, supersaturation is considered to be the driving force behind crystallization, there also has to be the presence of very tiny solid bodies, seeds, or nuclei to serve as a source for crystallization [3]. The nucleation mechanism in principle can be divided into primary and secondary nucleation. The idea is such that nucleation can either happen in the presence or absence of crystalline matter or surfaces such as crystals, crystallizer walls, and impellers. The focus of this work is primarily based on primary nucleation and therefore secondary nucleation is not considered. Nucleation in the absence of crystalline mater (i.e., primary nucleation) can be possible in two ways, thus homogeneous and heterogeneous nucleation.

2.1.4. PRIMARY NUCLEATION

HOMOGENEOUS NUCLEATION

In the absence of solid particles high energy is required for homogeneous nucleation to occur which makes it a rare process [41]. Nevertheless, homogeneous nucleation occurs when constant molecular collision due to fluctuations in the local concentration causes the formation of ordered clusters. A cluster is basically a group of several nanoscopic solute molecules. The attachment and detachment of single molecules to and from the cluster is what is known as Szilard mechanism [42]. Furthermore, the dynamics of cluster formation during nucleation is described by classical nucleation theory (CNT). According to CNT, fluctuations in density and other factors leads to the formation of clusters in which the resulting crystal nuclei have the same shape as a mature crystal [43]. The theory assumes that cluster formation is by an additive mechanism where clusters evolve in size by addition of single solute molecules [3, 44]:



where A is a single solute molecule, A_{n-1} is a cluster of two or more molecules, and A_n is a critical cluster.

The geometry of a cluster in terms of dimension, L , can be defined by using the area and volume shape factors, thus β and α respectively [45]. Hence, the cluster volume (V) and area (A) can be defined as shown in Eq. 2.7 and 2.8.

$$V = \alpha L^3 \quad (2.7)$$

$$A = \beta L^2 \quad (2.8)$$

The process of cluster formation can be described thermodynamically using Gibbs free energy. The overall excess free energy required for the formation of a new phase is defined as the sum the surface excess free energy (ΔG_S) and the volume excess free energy (ΔG_V) as shown in Eq. 2.9. ΔG_S is the free energy required for the formation of a cluster surface. Similarly, ΔG_V is the excess free energy required for the phase transformation. Also, γ is the interfacial tension between the developing crystalline surface and the supersaturated solution [3, 45].

$$\Delta G = \Delta G_S + \Delta G_V = \beta L^2 \gamma + \alpha L^3 \Delta G_V \quad (2.9)$$

The excess free energy is however, defined by assuming that a cluster will have a spherical shape. Therefore, the volume and area will be dependent on the radius rather than length. In that case, Eq. 2.9 is written accordingly as shown:

$$\Delta G = 4\pi r^2 \gamma + \frac{4}{3}\pi r^3 \Delta G_v \quad (2.10)$$

where ΔG_s is proportional to the square of the cluster radius (r^2), ΔG_v is proportional to r^3 , and ΔG_v is the Gibbs free energy per unit volume [46].

The formation of a nuclei depends on the competition between ΔG_s and ΔG_v . As seen in figure 2.4, when the cluster size is less than the critical size ($r < r_c$), the ΔG_s term dominates causing an initial increase in the overall excess free energy (ΔG). The cluster basically becomes unstable and subsequently dissolves [44]. Contrariwise, when $r > r_c$, ΔG_v dominates, (since solid state is more stable than liquid state), causing the overall excess free energy to go through a maximum at the critical radius. Beyond which the overall excess free energy (ΔG) becomes negative resulting in a stable and continuous cluster growth.

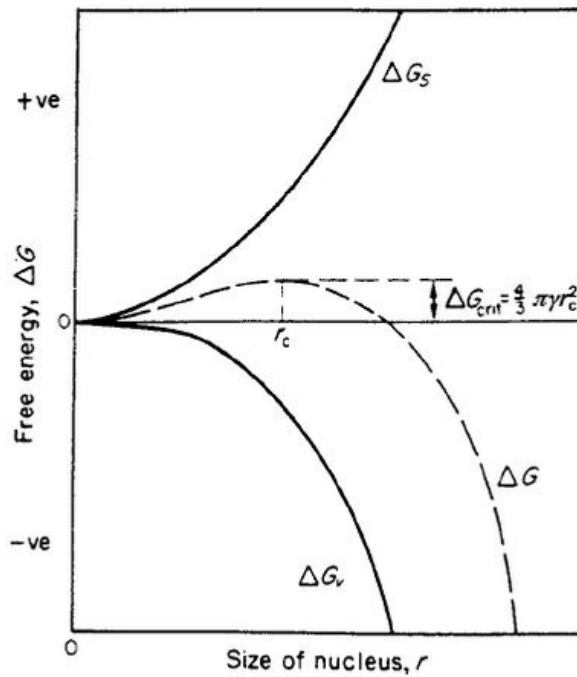


Figure 2.4: Free energy diagram explaining the concept of critical radius and energy [3]

The critical size (r_c) beyond which the nucleation occurs can be determined by differentiating Eq. 2.10 with respect to r and setting it to zero as shown below.

$$\frac{d\Delta G}{dr} = 8\pi\gamma r + 4\pi r^2 \Delta G_v = 0 \quad (2.11)$$

$$r_c = -\frac{2\gamma}{\Delta G_v} \quad (2.12)$$

The critical Gibbs free energy (ΔG_{crit}) which is the amount of energy required to form a stable nucleus can then be determined by substituting ΔG_v from Eq.2.12 in Eq.2.10.

$$\Delta G_{crit} = \frac{4\pi\gamma r_c^2}{3} \quad (2.13)$$

The rate of nucleation (J) is defined as the number of nuclei that form from a supersaturated solution per unit time per unit volume. It is a temperature dependent reaction rate and can be simply modelled using Arrhenius equation as shown in Eq.2.14. Furthermore, a relation between supersaturation and cluster size

can be described using Gibbs-Thomson equation which is given in Eq.2.15 [45], where v is the molecular volume, k is the Boltzmann constant and T is the absolute temperature.

$$J = A \exp\left(-\frac{\Delta G_{\text{crit}}}{kT}\right) \quad (2.14)$$

$$\ln(S) = \frac{2\gamma v}{kTr} \quad (2.15)$$

Substituting r_c with r from Eq.2.15 into Eq.2.13 we obtain

$$\Delta G_{\text{crit}} = \frac{16\pi\gamma^3 v^2}{3(kT\ln(S))^2} \quad (2.16)$$

According to CNT, the homogeneous nucleation rate of a crystal can now be expressed by substituting Eq.2.16 in Eq.2.14

$$J = A \exp\left(-\frac{\Delta G_{\text{crit}}}{kT}\right) = A \exp\left(-\frac{16\pi\gamma^3 v^2}{3(kT\ln(S))^2}\right) = A \exp\left(-\frac{B}{(\ln(S))^2}\right) \quad (2.17)$$

where A and B are the kinetic and thermodynamic parameters respectively.

HETEROGENEOUS NUCLEATION

In practical terms, the presence of impurities such as dust during crystallization is inevitable. Nucleation in the presence of such foreign materials is termed as heterogeneous. This type of nucleation mechanism proceeds faster compared to homogeneous nucleation. The formation of a nuclei on a surface or an interface basically lowers the crystal nucleation work (W^*) (i.e., energy barrier for nucleation) or ΔG_{crit} , which is as a result of a reduced interfacial tension (γ in Eq.2.16)[6]. In other words, the reduced interfacial tension creates an energy barrier which is lower for heterogeneous nucleation compared to homogeneous nucleation [47] as shown in figure 2.6.

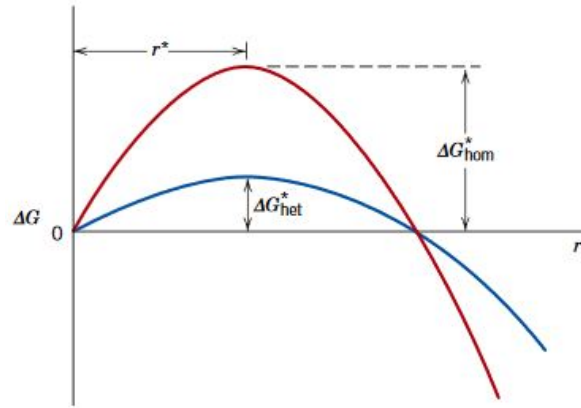


Figure 2.5: Comparison between ΔG_{crit} (i.e., ΔG^*) for homogeneous and heterogeneous nucleation [6]

This reduced interfacial tension in heterogeneous nucleation is known as effective interfacial tension (γ_{eff}). It includes the different interfacial tension between the nucleus and supersaturated solution (γ), nucleus and heterogeneous particle (γ_{pn}), and the supersaturated solution and heterogeneous particle (γ_{ps}). The relation between the effective interfacial tension and the interfacial tension can be represented as:

$$\gamma_{\text{eff}} = \psi\gamma, \quad (2.18)$$

where ψ is the activity factor and ranges between zero and unity [43].

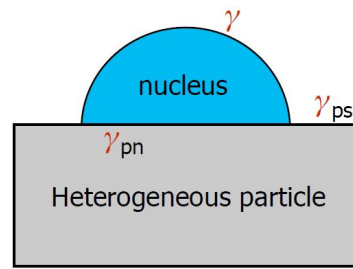


Figure 2.6: A schematic representation for heterogeneous nucleation.

In terms of nucleation thermodynamics, the exponential parameter, B , simply reflects the structure of the nucleus and describes the nucleation work or the free energy barrier and are related as shown in Eq.2.19 [43].

$$\frac{W^*}{kT} = \left(\frac{4c^3 v^2 \gamma_{eff}^3}{27(kT)^3 (\ln(S))^2} \right) = \left(\frac{B}{(\ln(S))^2} \right) \quad (2.19)$$

where the shape factor $c = (36\pi)^{1/3}$. This expression is valid for heterogeneous nucleation. In the case of homogeneous nucleation, the effective interfacial tension (γ_{eff}) is replaced with interfacial tension (γ). A smaller B value suggests that nucleation work is lower and nucleation proceeds faster.

On the other hand, the pre-exponential parameter, A , describes the nucleation molecular kinetics [43]. It also describes the statistical process by which a building unit attaches to the nucleus [47]

$$A = z f^* C_0 \quad (2.20)$$

where z is the Zeldovich factor, f^* is the attachment frequency, and C_0 is the concentration of nucleation sites. The Zeldovich factor means that there is a possibility of cluster dissolution even though it is larger than the nucleus size [47]. A large A value either indicates a higher number of possible active nucleation sites or a higher attachment frequency.

2.1.5. INDUCTION TIME AND MODELS

Induction time refers to the mean time gap between which supersaturation of a solution is reached and the appearance of a new phase. The term 'new phase' always refers to the detectable solid crystal found in solution. One of the conventional methods for determining induction time is the use of Crystalline which is carried out on macro-scale. The mode of operation is solely dependent on light transmissibility. A reduction in light transmissibility indicates the presence of a crystal in the solution. That moment of reduced transmissibility is defined as the induction time.

In contrast, the method used in this research was simply based on using a microscope camera to detect crystals in microfluidic droplets. During induction time measurements, time lapse images of droplets were taken and analysed to determine the very moment a crystal forms.

CONVENTIONAL MODEL

The calculation and analysis of Induction times can be done in two ways. The first is a conventional method which basically assumes that the volume fraction of crystalline phase in a suspension is only possible by primary nucleation and growth. In essence, the induction time is related to the crystal volume fraction (α), linear growth rate (G), and nucleation rate (J) as shown in Eq 2.21. Some assumptions used for this model was that particles formed were spherical and had a linear growth rate. Certain assumptions for G and α values led to variations of 5 orders of magnitude for induction times of 4-hydroxy acetophenone in ethyl acetate [47].

$$t_i = \left(\frac{3\alpha}{\pi G^3 J} \right)^{1/4} \quad (2.21)$$

SINGLE NUCLEATION MECHANISM MODEL

The second model is a stochastic model that is capable of determining kinetic parameters such as nucleation rates from induction times. This model is based on the single nucleation mechanism where a single crystal causes the formation of all other crystal by secondary nucleation. In this work, an extension of this model was used for a microfluidic system where nucleation of crystals occurred in droplets. Every droplet is considered as an independent experiment and the probability of finding m nuclei within a particular time gap is described by the Poisson distribution 2.22 [48].

$$P_m = \frac{N^m \exp(-N)}{m!}, \quad (2.22)$$

where N represents the expected average number of nuclei formed within a specific time frame. In a situation where no nuclei are formed, thus $m=0$, then Eq 2.22 can be written as Eq 2.23. On the other hand, if a certain amount of nuclei are formed in individual droplets, thus $m \geq 1$, then the probability $P_{\geq 1}$ is simply expressed as Eq 2.24

$$P_0 = \exp(-N) \quad (2.23)$$

$$P_{\geq 1} = 1 - P_0 = 1 - \exp(-N) \quad (2.24)$$

Eq 2.24 can further be expanded by introducing the nucleation rate (J), volume of individual droplets (V), and the specific time interval (t_j). The product of these parameters can be related to the average number of nuclei formed (N) as shown in Eq 2.25. Therefore, the probability that more than one nuclei are formed is given as Eq 2.26.

$$N = JVt_j \quad (2.25)$$

$$P(t_j) = 1 - P_0 = 1 - \exp(-JVt_j) \quad (2.26)$$

In a situation where a crystals are only detected in the form of suspension in the solution, then the specific time interval (t_j) can be said to include the overall detection time (t) and the time taken for crystal to grow until detection also known as delay time (t_g) as shown.

$$t_j = t - t_g \quad (2.27)$$

In order to dimensionalize Eq 2.26, Eq 2.27 and a mean induction time scale (τ) are introduced as given below.

$$P(t) = 1 - \exp\left(-\frac{t - t_g}{\tau}\right), \quad (2.28)$$

where $\tau = \frac{1}{JV}$.

Equation 2.28 is only valid for instances where $t \geq t_g$. More often than not the delay time is ignored as it is insignificant compared to the mean induction times. The inclusion of t_g yielded strange fittings in previous work, hence it was not used here. The exclusion of t_g also resulted in bad fits therefore another model known as the Weibull model was used.

The Weibull model is also an exponential model but with an extension. It is a two-parameter distribution function where the mean induction time scale parameter (τ) is related to the median nucleation time (t_{MED}) as shown [49].

$$\tau = t_{MED} (\ln 2)^{1/k} \quad (2.29)$$

$$P(t) = 1 - \exp\left[-\left(\frac{t}{\tau}\right)^k\right] \quad (2.30)$$

The k parameter gives information about an increasing or decreasing nucleation. When $k > 1$, the nucleation rate increases with time. But when $k < 1$, the nucleation rate decreases with time. Also, larger k values signify a longer initial plateau at the start of nucleation [49].

EXPERIMENTAL PROBABILITY CALCULATION

There are large variations in the detection of crystals in individual droplets. Therefore, in order to determine the probability, a large number of induction time measurements are required specially at constant conditions such as concentration, temperature and droplet volume. As mentioned earlier on, every single droplet is considered as an isolated experiment. Hence, the probability distribution $P(t)$ can be determined using Eq 2.31 [50].

$$P(t) = \frac{M^+(t)}{M}, \quad (2.31)$$

where $M^+(t)$ is the number droplets containing detectable crystals at time t and M is total number of droplets. A fit to the Weibull model shows a very good correlation between the model and the experimental data.

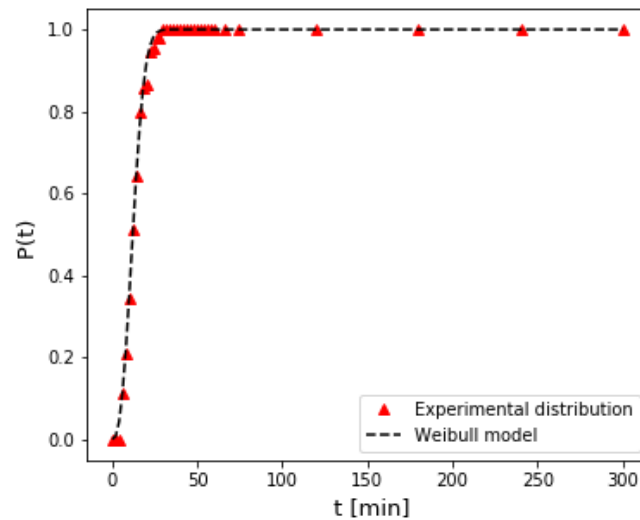


Figure 2.7: Experimentally determined probability distributions $P(t)$ of induction times. Dotted lines are fits to Eq 2.30

3

RAMAN

3.1. RAMAN SPECTROSCOPY

The complex nature of artificial urine gives many possibilities of forming different crystals different from the intended calcium oxalate (CaOx) crystals. For this reason, it is very important to ensure that CaOx crystals are formed when CaCl_2 and NaOx compounds are mixed in artificial urine. Generally, calcium oxalate consists of two carbon atoms and one calcium atom. However, COM has one water molecule whereas COD has two water molecules. A visual microscope inspection of the morphology of these crystals in artificial urine is not conclusive enough. Hence, analytical instrumentation (Raman spectroscopy) was employed to determine the vibrational mode or structural fingerprint of the different CaOx phases in artificial urine. Raman spectroscopy can be used for both qualitative and quantitative analysis. The later was rather used by determining the intensity and the wavenumber shift of scattered radiation.

3.1.1. QUANTITATIVE APPROACH

When a crystal is exposed to a laser beam (monochromatic light), most of the light is absorbed. A small portion of this light, however, gets scattered elastically or inelastically. When the frequency of the scattered light or photon ω_s is equal to the frequency of the incident light or photon ω_i , it leads to a process called Rayleigh scattering. This type of scattering provides no useful information. On the other hand, a change in frequency is called Raman Scattering or Raman Effect [7]. This effect is purely dependent on the chemical structure of the analyte. The Raman scattering can be described as a two-photon process. When an electron within the crystal lattice absorbs energy, it rises to a virtual state of energy. The electron loses energy and falls back to either its initial energy level or to a different energy level in the process emits a new photon. Depending on the final vibrational energy level of the electron Raman scattering can be divided into Stokes and anti-Stokes lines or bands.

Stokes bands are Raman bands which occurs when the energy of the scattered photon is less than that of the incident photon [7, 51], which in this case yields a positive transition energy. The energy of the scattered photon can therefore be described by the following equation

$$h\omega_s = h\omega_i - h\omega_M \quad (3.1)$$

Contrariwise, when the energy of the scattered photon is higher than that of the incident photon the Raman bands are referred to as anti-Stokes bands [51]. In this scenario, the energy of the scattered photon is rather described by the following equation

$$h\omega_s = h\omega_i + h\omega_M \quad (3.2)$$

Raman spectrum is very important in identifying different compounds in a system. A spectra, for instance, consist of many peaks with each peak corresponding to a molecular bond vibration. Each bond type such as C-C, C=C, O-H, O-C-O, etc., has a unique vibrational mode which leads to specific interactions with light and hence produce different Raman shifts [52]. Raman peaks are usually represented such that the Raman shift or wavenumber shift $\Delta\nu$ (unit: cm^{-1}) and intensity lie on the abscissa and the ordinate respectively [7]. The

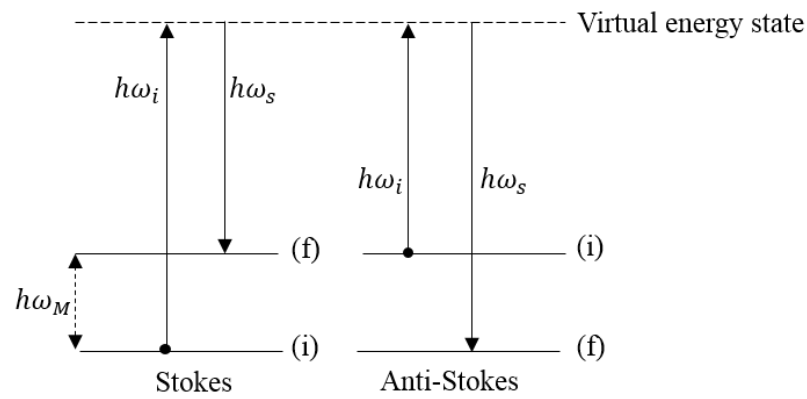


Figure 3.1: The energy transition process in Stokes (left) and Anti-Stokes (right) Raman scattering. The (i) denotes initial energy state, whereas (f) denotes the final energy state.

wavenumber shift is basically the same as the transition frequency as seen earlier on as ω_M [7]. The intensity of a spectrum is seen to be proportional to the concentration. With mixtures, relative intensities provides information about relative concentration of the components [53]. A positive wavenumber shift represents Stokes Raman scattering, whereas a negative wavenumber represents anti-Stokes Raman scattering as seen in figure 3.1. A representation of Rayleigh and Raman spectra. It must also be noted that only Stokes Raman bands were studied in this work.

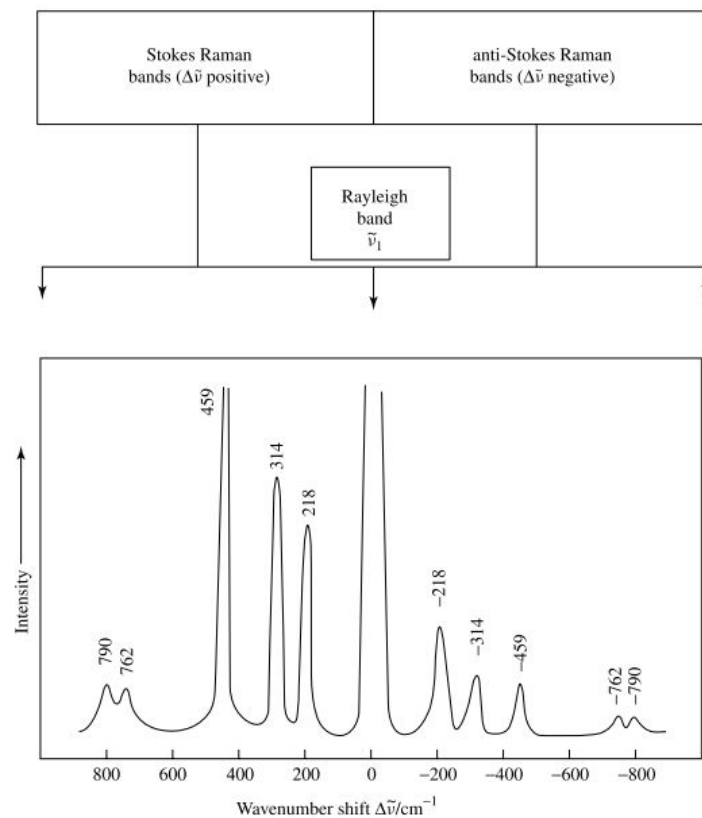


Figure 3.2: A representation of Rayleigh and Raman spectra showing the positive and negative values of [7]

3.2. MATERIALS AND METHODS

The experiments were performed using Raman Rxn2 analyzer in conjunction with a phase-optimized sampling probe to monitor laboratory scale batch samples. A schematic of the setup has been provided in the figure below.

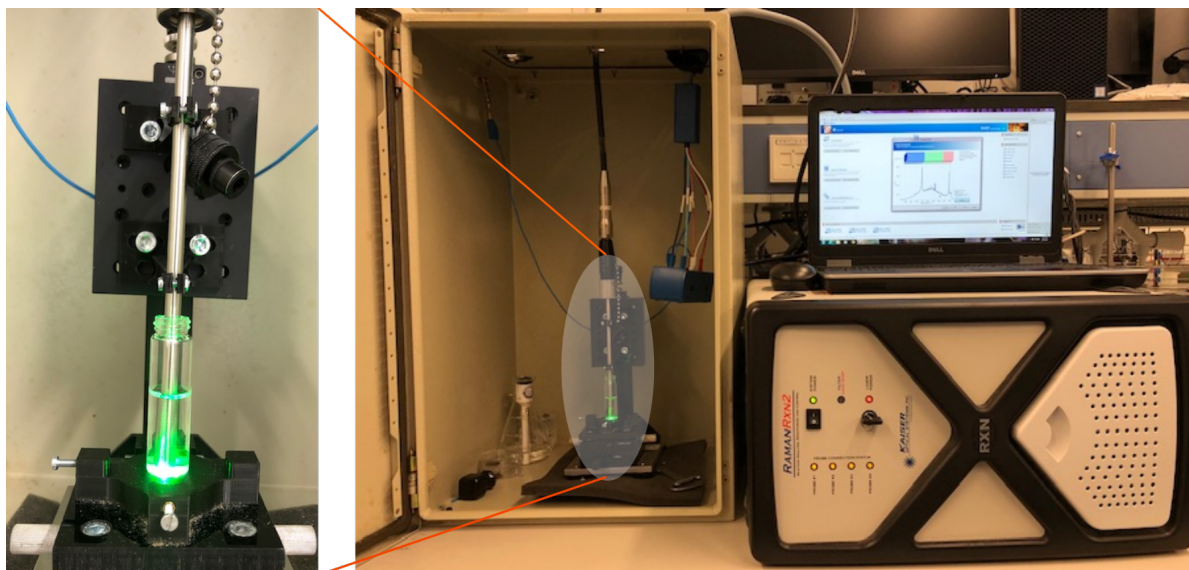


Figure 3.3: Raman Rxn2 analyzer with phase-optimized sampling probe

All samples under study were prepared in a 4ml artificial urine solution contained in an 8ml glass vial. In order to setup the device for measurements the following procedure was undertaken.

1. The probe was inserted into the excitation laser which is located in the faraday chamber. In order to do so the rim was loosened, the probe was then inserted and tightened to keep it firmly in place.
2. The 8ml glass vial was placed inside the faraday chamber while lowering the probe in to the sample. The chamber is then closed. The position of the probe needs to be adjusted with respect to solids in the solution, in order to obtain the best focus.
3. The analyzer beside the faraday chamber was switched on by the turning the key in a clockwise matter (a red light pops up).
4. The 'ic-Raman' program on the computer was opened.
5. The experiment name, interval time (usually 2 minutes), and interval time (10 seconds) were input. There was no need to select a reference spectra.
6. Before running the experiment, the exposure efficiency needed to be checked. An exposure time of 15 seconds usually gave an efficiency in the green zone. This meant that there was enough time for the detector to be exposed to the Raman signal for better to signal-to-noise ratio.
7. The play button of then pressed to initiate measurements.
8. Once the experiment was done, the second button above the resulting graph which is the 'copy as text' option was selected.
9. The copied text was then pasted in notepad and saved for further analysis.

Raman spectra for COM (supplier) and CaOx as well as different artificial urine filtrates were obtained. All experiments were done at room temperature.

Table 3.1: Equipment used for Raman spectroscopy experiments

Equipment	Equipment name	Brand
Scale	-	Mettler Toledo
Raman spectrometer	Kaiser Raman RXN2	Kaiser Raman
Sonicator	2510 Ultrasonic Cleaner	Branson

Table 3.2: Amount of chemicals used for preparation of artificial urine (AU)

Compound name	Chemical formula	Concentration (mM)	mg/50ml ultrapure water
Sodium chloride	NaCl	90	263.0
Potassium chloride	KCl	42	156.6
Ammonium chloride	NH ₄ Cl	20	53.5
Creatinine	C ₄ H ₇ N ₃ O	7	45.9
Urea	CH ₄ N ₂ O	300	900.9
Tri-sodium citrate	Na ₃ C ₆ H ₄ O ₇	2	25.8
Magnesium sulfate heptahydrate	MgSO ₄ • 7H ₂ O	2	24.6
Sodium sulphate	Na ₂ SO ₄	13	92.3
Sodium phosphate monobasic	NaH ₂ PO ₄	16	96.0

Table 3.3: Amount of chemicals required to prepare samples in AU for Raman spectroscopy experiments

Compound	Final concentration (mM)	Vendor
CaCl ₂	4.3, 6.0	Sigma-Aldrich
Na ₂ C ₂ O ₄	1.2, 4.3	Sigma-Aldrich
COM powder	22.8	Alfa Aesar

3.3. PREPARATION PROCEDURE OF SAMPLES FOR RAMAN ANALYSIS

3.3.1. PREPARATION OF ARTIFICIAL URINE

The chemicals used in this experiment as seen in table 3.2 were of purity greater than or equal to 98%. Each chemical was weighed using a weighing paper and poured into a 100ml conical flask. 50 ml of ultrapure water was weighed to ensure accurate volume and then added to the chemicals in the 100 ml conical flask. The flask was covered with parafilm and sonicated for 25 to 30 minutes to ensure complete dissolution of the chemicals. This solution formed the basis for further addition and dissolution of other chemicals such as calcium chloride, sodium oxalate, and COM powder (supplier). It was also used within a 12 hour period to avoid dissociation of urea into ammonia and other instabilities that may occur.

3.3.2. COM (SUPPLIER)

100 mg of COM powder from Alfa Aesar was weighed and poured into 30 ml of AU contained in a 100 ml Easymax reactor. The solution was then stirred for an hour. The COM in this case did not completely dissolve. 4 ml of the colloidal suspension was drawn using a 5 ml micropipette into an 8 ml glass vial which was immediately analyzed under Raman spectroscope.

3.3.3. CaOx ([Ca]=4.3mM, [Ox]=4.3mM)

CaOx crystals were precipitated from an equal molar concentration of calcium chloride and sodium oxalate. 8.6 mM concentration of CaCl₂ was prepared by dissolving 19.1 mg of the compound in 20 ml of freshly prepared AU. The same concentration was prepared for NaOx where 23 mg of NaOx was dissolved in 20ml of AU. The dissolution of both compounds was done using a sonicator for 15 minutes. Prior to precipitation, both solutions were filtered using 0.45µm pore filter. A micropipette was used to draw 2 ml of each solution and mixed together in an 8ml glass vial. The final concentration for CaCl₂ and NaOx in AU after mixing was 4.3 mM. The vial was covered with a lid gently turned up and down three times to ensure a homogeneous mixture. The 4 ml solution was allowed to stand overnight for precipitation.

3.3.4. CaOx ($[\text{Ca}]=6.0\text{mM}$, $[\text{Ox}]=1.2\text{mM}$)

CaOx was precipitated from an unequal molar concentrations of calcium chloride and sodium oxalate in artificial urine. The same procedure in 3.3.3 above was repeated here but with different molar concentrations of CaCl_2 and NaOx . In this case, 12 mM concentration of CaCl_2 was prepared by dissolving 26.6 mg of the compound in 20 ml of freshly prepared AU. 2.4 mM concentration of NaOx was prepared where 6.4 mg of NaOx was dissolved in 20 ml of AU. The final concentration for CaCl_2 and NaOx in AU after mixing was 6.0 mM and 1.2 mM respectively.

3.3.5. ARTIFICIAL URINE FILTRATE FROM COM (SUPPLIER) SOLUTION

20 ml of the COM (supplier) sample (as prepared in 3.3.2 above) was poured into a 50 ml self-standing plastic test tube. The suspension was centrifuged at 7500 rpm for 15 minutes and filtered using a $0.45\mu\text{m}$ pore filter. The filtrate, thus artificial urine which now contains soluble calcium and oxalate was then analyzed for Raman bands.

3.3.6. ARTIFICIAL URINE FILTRATE FROM CaOx SOLUTION

CaOx crystals in section 3.3.3 and 3.3.4 above were filtered using a $0.45\mu\text{m}$ pore filter AU after centrifuging the solution at 7500 rpm for 15 minutes. 4 ml each of saturated AU containing dissolved calcium and oxalate were collected using a micropipette into two separate 8 ml glass vials and sent for Raman analyses.

3.4. RESULTS

A Raman spectrum with wavenumber shift spanning from $380\text{--}1800\text{ cm}^{-1}$ was studied. In order to avoid analysing any background interference, a Raman spectra was obtained for the different artificial urine filtrates as seen in figure 3.4. AU filtrates (blue, black and green lines) contained undersaturated levels of calcium and oxalate. AU (SS=0) contained no calcium and oxalate. The resulting peaks for all samples were observed at the same Raman shift.

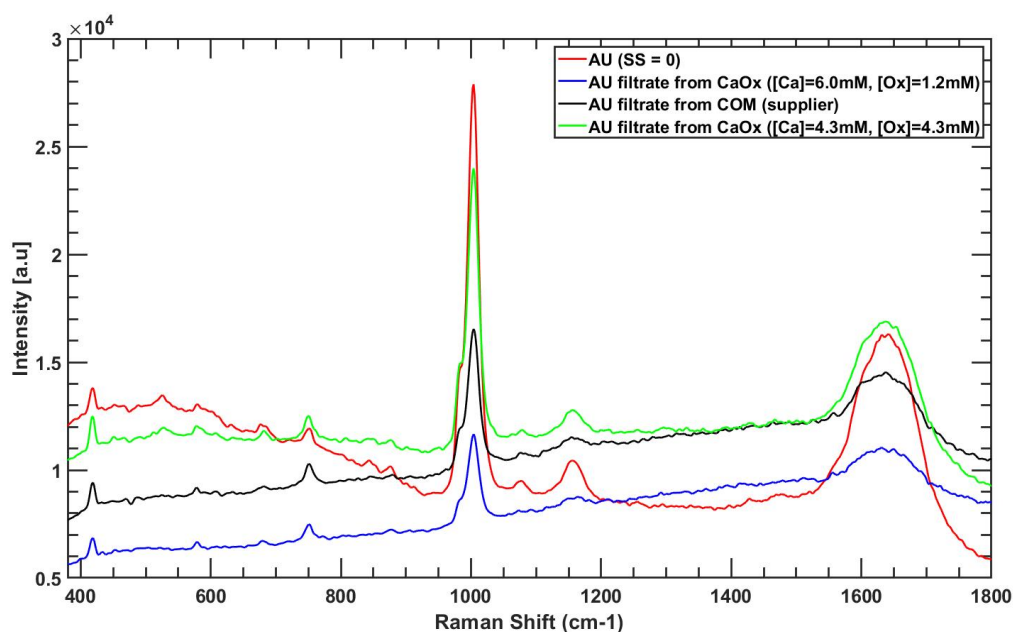


Figure 3.4: Raman spectra of artificial urine filtrates

For a clearer distinction, the spectrum of AU filtrate from CaOx solution ($[\text{Ca}]=6.0\text{mM}$, $[\text{Ox}]=1.2\text{mM}$) was compared with the spectra of COM (supplier) and CaOx crystals in figure 3.5. This spectra demonstrated 3 distinct peak regions A, B, and C which were common to the peaks observed in figure 3.4. In the other words, these peaks were primarily due to the dissolved compounds contained in the artificial urine.

For easy representation of results, figure 3.5 is subdivided into two parts. The first part (i.e. figure 3.6) has

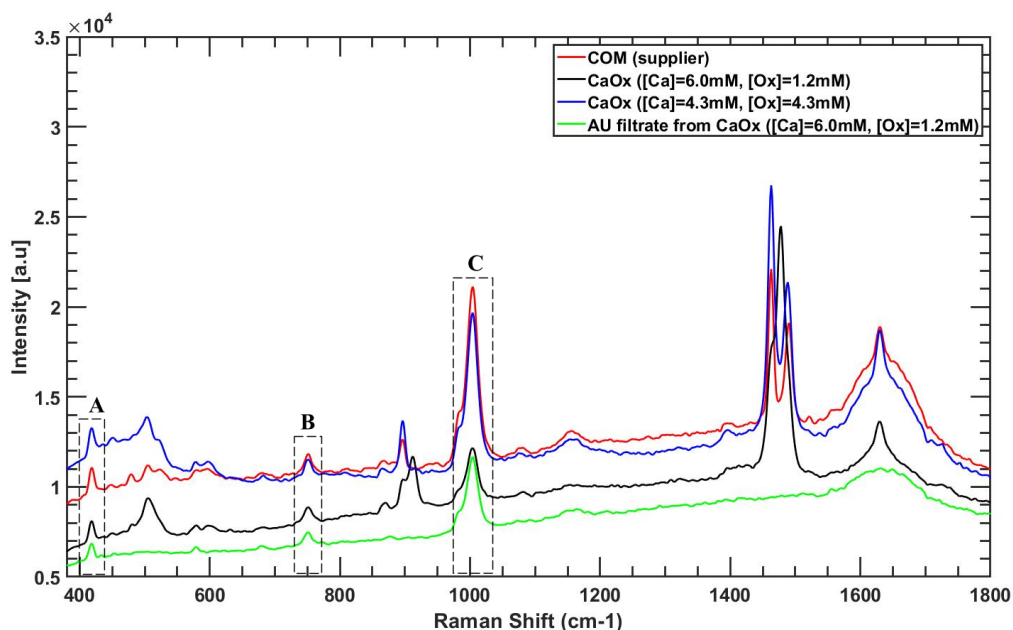


Figure 3.5: Raman spectra showing significant spectral difference which allows COM (supplier) and CaOx peaks to be distinguished from any background noise (i.e. artificial urine-AU)

the wavenumber shift spanning from 380 - 1100 cm^{-1} , whereas the second part (i.e. figure 3.7) spans from 1100 - 1800 cm^{-1} . A summary of the comparison between this work and literature for the most prominent peaks have also been presented in table 3.4

Table 3.4: Comparison of between thesis study and literature Raman bands

Present study			Literature values [54–58]	
COM (supplier)	CaOx		CaOx	
	COM	COD	COM	COD
504	504	-	503, 504, 506	507, 508
896	896	-	896, 897	-
-	-	912	-	910, 912
1463	-	-	1462, 1463, 1465	-
-	-	1478	-	1474, 1477, 1478
			1487, 1488, 1489, 1490, 1492	
1490	-	-		-
1630	1630	-	1630, 1631	1632

The most prominent Raman bands observed in kidney stones for both COM and (COD) are reported to be at 504, 897 (898), 1465, 1491, and 1630 (1632) cm^{-1} [54]. These bands are at similar wavenumber shifts as those observed in figure 3.6 and 3.7. This suggests that the precipitated crystals are entirely made of COM and COD. Peaks at 504 and 896 cm^{-1} as observed in figure 3.6 are characteristics of COM, and are assigned the O-C-O deformation mode and the $\nu(\text{CO})$ stretching mode respectively [54]. The $\nu(\text{CO})$ stretching mode in the pure state COD also occurred at 912 cm^{-1} [54].

Figure 3.7 shows the key absorption peaks which are usually used to distinguish between the two calcium oxalate hydrates. A doublet peak at 1463 and 1490 cm^{-1} are the main absorption peak for COM, and are described by the $\nu(\text{CO})$ stretching mode [55, 56]. On the other hand, a singlet peak at 1478 cm^{-1} shows the presence of COD which is assigned the $\nu(\text{CO})$ stretching [57, 58]. Lastly, a less intense peak occurring at 1630 cm^{-1} were assigned to CO asymmetric stretching for COM [58].

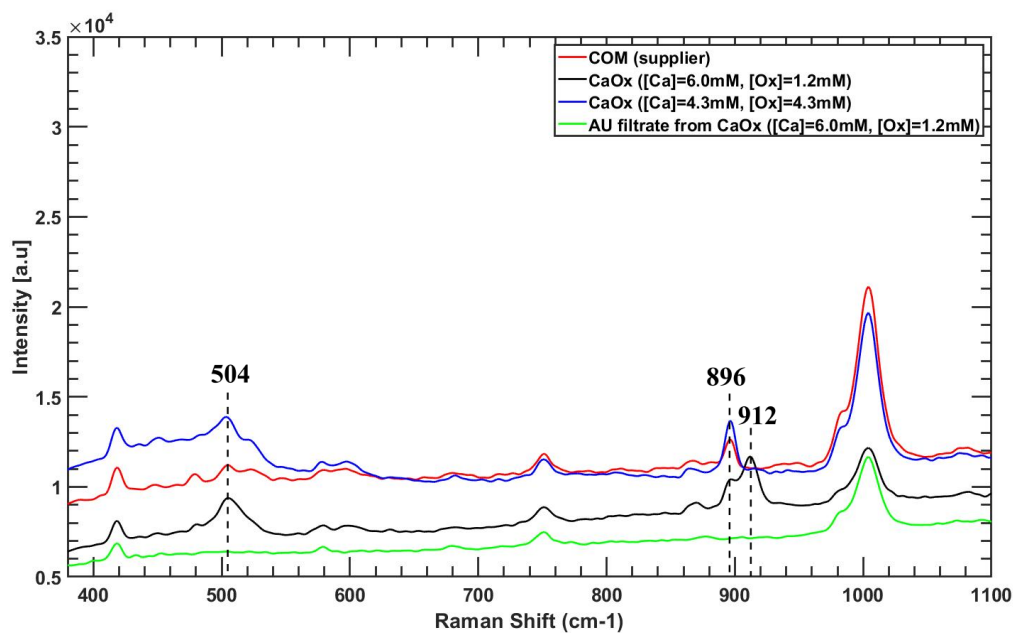


Figure 3.6: Raman spectra for COM and CaOx peaks within $380\text{--}1100\text{ cm}^{-1}$ region

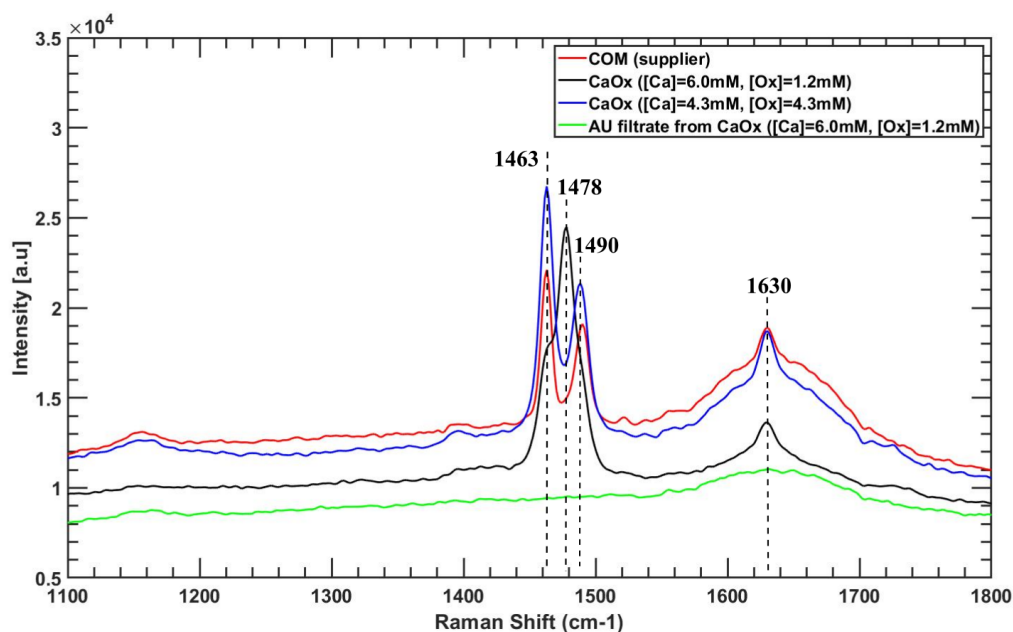


Figure 3.7: Raman spectra for COM and COD peaks within $1100\text{--}1800\text{ cm}^{-1}$ region

3.5. DISCUSSIONS

In this work analysis of precipitated COM and COD in a bulk artificial urine solution has been presented. The spectra of these CaOx crystals were compared with that of COM powder from a supplier and very much showed similarities. Aside from the Raman spectra, microscope images of the samples from the aforementioned conditions were obtained after 3 hours to give a clearer and a possible reasoning for the position of the peaks.

The peaks for COM, (COD) considered were those at 896, (912), 1463, (1478), and 1490 cm^{-1} as shown

previously in figure 3.6 and 3.7. The spectra for CaOx (black line) shows predominant COD peaks, whereas the spectra for CaOx (blue line) shows predominant COM peaks.

As seen in figure 3.8, the sizes of COD are relatively larger compared to COM when the unequal molar ratio of calcium and oxalate is used. This may perhaps make COD crystals easily detectable and hence, the reason why COD peaks were predominant under this condition. Of course, one can also assume that at non-equimolar ratios, the amount of COD formed is significantly higher than that of COM which may also explain the predominant appearance of COD peaks

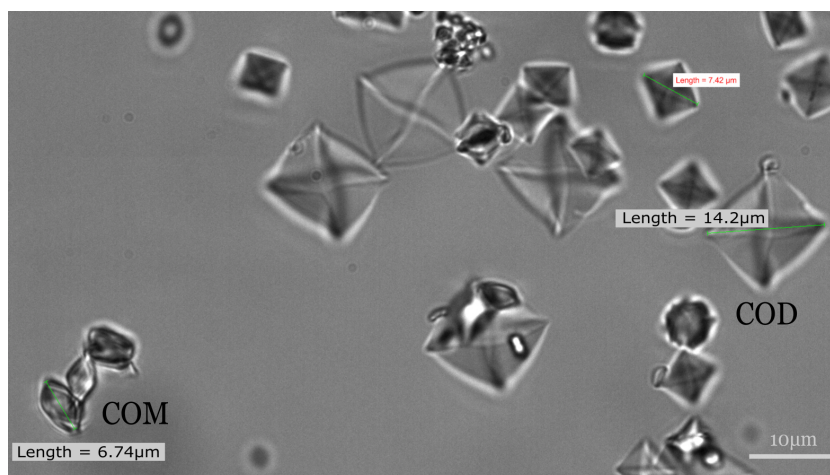


Figure 3.8: The polymorphic forms of calcium oxalate crystals in artificial urine obtained under non-equimolar conditions of $[\text{CaCl}_2] = 6.0\text{mM}$ and $[\text{NaOx}] = 1.2\text{mM}$.

On the other hand, as the molar ratio of calcium and oxalate becomes 1, the volume of COM and COD crystals become maximal which was also shown by Robertson et al. [59]. COM peaks were predominant under this condition, and this may have been due to a considerable increase in size of COM crystals. This is however, less likely since both COM and COD sizes were very similar as seen in figure 3.9. Another reason may have been due to a relatively higher number of COM crystals compared to COD.

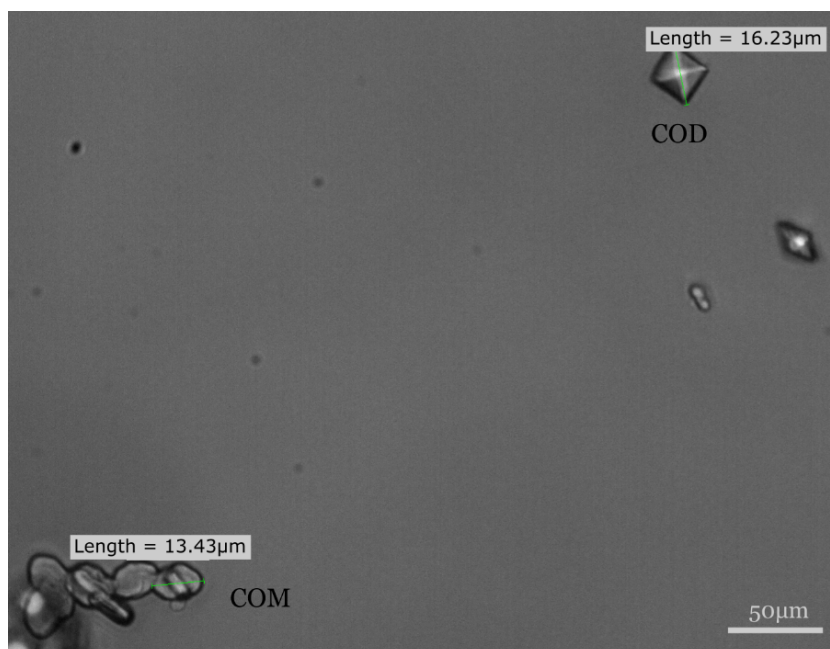


Figure 3.9: The polymorphic forms of calcium oxalate crystals in artificial urine obtained under equimolar conditions of $[\text{CaCl}_2] = 4.3\text{mM}$ and $[\text{NaOx}] = 4.3\text{mM}$.

4

POLARIZED LIGHT MICROSCOPY

It is very difficult to distinguish between calcium oxalate polymorphs, especially at the onset of nucleation when using bright field microscopy. This is due to the fact that crystals are still tiny and that their morphologies are impossible to identify. An effective way to detect and differentiate between these polymorphs is by their optical properties. Birefringence, for that matter, is an optical property of a material whose refractive index depends on light propagation or polarization. In other words, birefringence can be defined as the difference in refractive index between the ordinary and extraordinary rays. Depending on the refractive index, a crystal may tend to exhibit a strong or faint birefringence under crossed polarized light.

Polarized light microscopy is a good contributory method used by many scientists to determine the birefringence of calcium oxalate crystals [60, 61]. For induction time measurements, this method was practically used to differentiate between COM and COD in a microfluidic setup. As seen in literature, COM predominantly shows strong birefringence [62], whereas, COD is seen to be only slightly birefringent [63].

4.1. BIREFRINGENCE OF CALCIUM OXALATE CRYSTAL UNDER POLARIZED LIGHT

For easy understanding of experiments performed under chapter 6, it is important to introduce the basic principle of birefringence. Although Figure 4.1 does not necessarily depict the experimental setup in the microfluidic experiments, it still provides a fair idea as to why some crystals appear bright and others not. When white light goes through the polarizer it becomes restricted to vibrations in only one plane. The in-plane polarized light then gets refracted by the anisotropic crystal into two components, ordinary and extraordinary rays. The resultant of these two rays then goes through the analyzer where the crystal can then be observed through the microscope eyepieces.

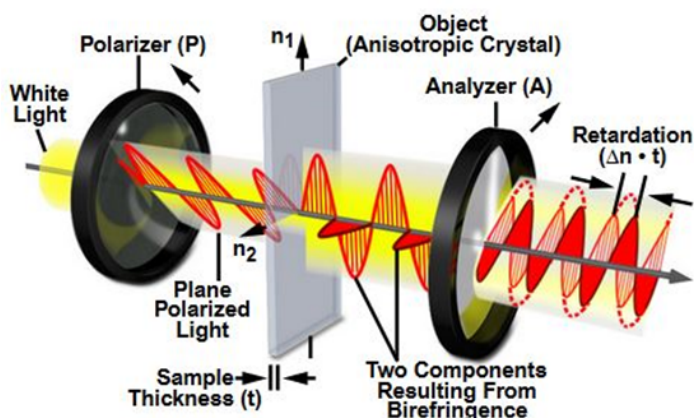


Figure 4.1: Birefringent crystal between crossed polarizers [8]

4.1.1.1. CROSSED POLARIZATION

Crossed polarization is a concept where a polarizer and an analyzer are oriented at right angles to each. With this configuration, the analyzer blocks the transmission of the plane polarized light as seen in figure 4.2. This creates a dark field of view which can be seen through the microscope eyepiece. When a birefringent crystal is then placed between the polarizer and analyzer it may appear bright or invisible depending on the orientation of its optical axis with respect to the polarizer.

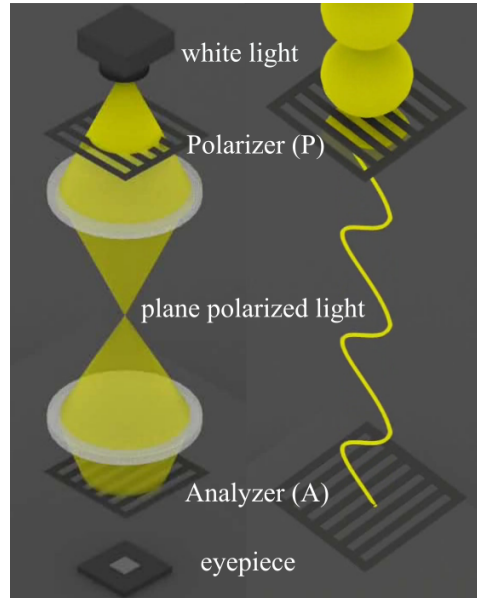


Figure 4.2: Schematic representation of crossed polarization

Figure 4.3 shows a birefringent crystal in between a polarizer and an analyzer with its optical axis aligned to the transmission azimuth of the polarizer. The light from the polarizer which subsequently goes through the crystal is not refracted into the ordinary (o) and extraordinary rays (e), hence the light basically vibrates in a plane parallel to the polarizer and perpendicular to the analyzer. This light then gets blocked by the analyzer and results in a situation where the crystal goes into extinction against the dark field of view.

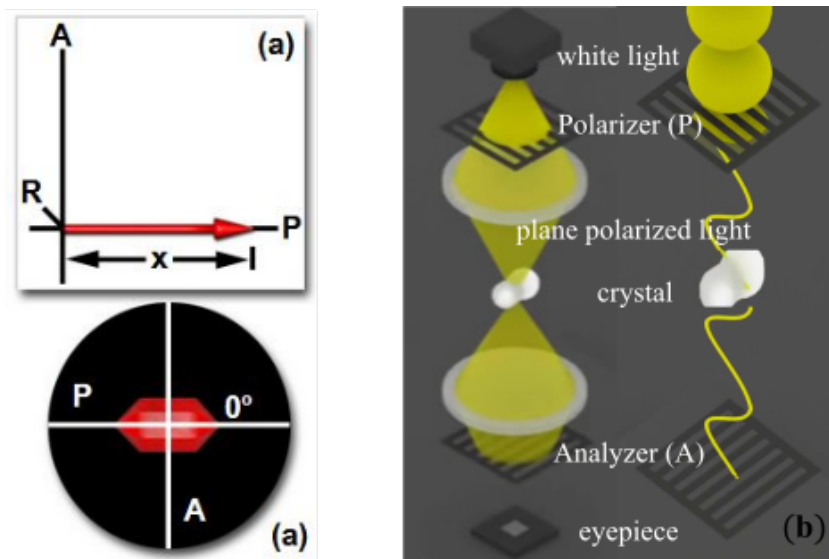


Figure 4.3: Orientation of a birefringent crystal under crossed polarized light with its optical axis aligned parallel to the transmission azimuth of the polarizer [8]

This can clearly be seen in figure 4.4 where the tetragonal COD in (a) appeared to be extinct in (b). During

this experiment the polarizer was aligned at a 0 degree angle making it perpendicular to the analyzer (i.e. cross polarization). COD crystal is uniaxial [64] which means that it has only one optical axis [65]. This makes it highly likely for COD to become extinct under such polarizer-analyzer configuration. In figure 4.4 (b), because the optical axis of COD became parallel to the polarizer, the polarized light went through the crystal without any diffraction. The undiffracted light gets blocked by the analyzer as it vibrates perpendicularly, rendering the COD crystal invisible in the microscope eyepiece.

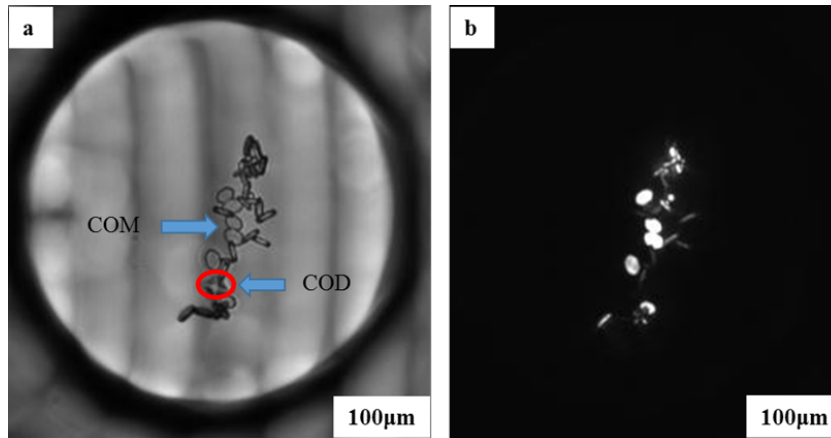


Figure 4.4: Polymorphic forms of calcium oxalate in a microfluidic droplet as seen under (a) white light and (b) crossed polarized light, using 20x objective lens and a polarizer angle of 0°.

Figure 4.5 shows a birefringent crystal placed between a polarizer and an analyzer with its optical axis aligned at an angle to the transmission azimuth of the polarizer. The light from the polarizer which passes through the crystal gets refracted into the ordinary (o) and extraordinary rays (e). The resultant R of the two rays vibrates in a plane at an angle to the analyzer. This light then gets through the analyzer and results in a situation where the crystal becomes fairly bright against the dark field of view. Maximum brightness will be seen if the crystal aligns itself at a 45° angle to the polarizer.

Some COM (monoclinic) in figure 4.4 appeared very bright while others appeared fairly bright. The optical axis of these COM crystals had to be aligned in a direction nonparallel to that of the polarizer for this to occur [66]. COM is biaxial and has two optical axis. Hence COM will most certainly appear bright or at least fairly bright under crossed polarization.

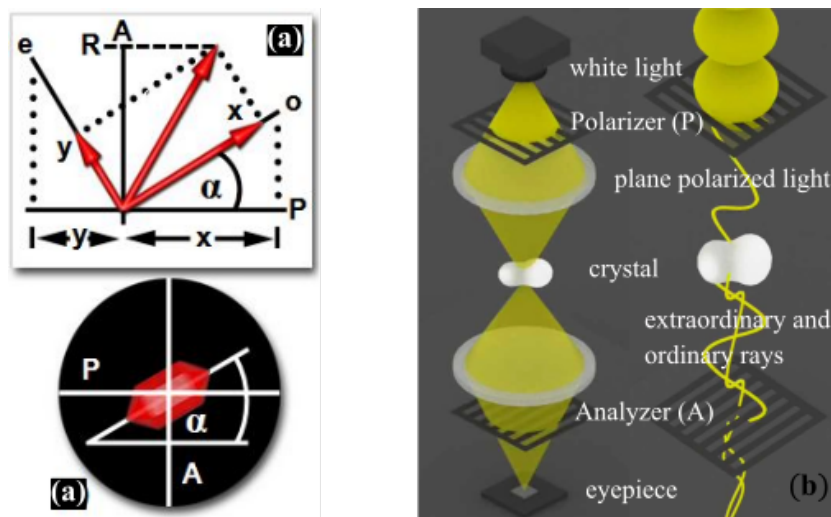


Figure 4.5: Orientation of a birefringent crystal under crossed polarized light with its optical axis aligned at angle to the transmission azimuth of the polarizer [8]

5

PRODUCTION OF DROPLET-BASED MICROFLUIDIC DEVICE

Emulsion or droplet-based microfluidic technology offers a range of advantages over large scale systems. Droplets generated through a microfluidic device are considered as microreactors, in which analytes are confined within a small volume, thereby reducing the amount of material consumed [67]. Enormous amount of experiments can also be performed within these microreactors under precisely controlled and identical conditions [68]. Furthermore, droplet-based microfluidics offers unique experimental approaches that are impossible or difficult to implement on a larger scale, such as molecular diffusion, heat transport and more extreme reaction conditions [69]. The production of such devices includes important processes such as hydrophobization, spin coating, semicuring and bonding.

EMULSIFICATION

Droplets formation is basically driven by the interfacial forces between the two immiscible phases. Interfacial forces are seen to be dominant over other forces such viscous, inertial, and gravitational forces during spontaneous droplet generation. A very important dimensionless number known as the capillary number Ca is always defined when it comes to microfluidic droplet generation. It basically defines the relation between viscous forces and interfacial forces. The capillary number can be changed by the adjustment of the continuous phase flow rate or dispersed phase flow rate [70]. In the case of Reynolds number, when $Re < 10$ a laminar flow regime exist. As such droplet production is very reproducible with less variations in size distributions [71].

5.1. MATERIALS AND METHODS

Table 5.1: Chemicals and materials used in making droplet-based microfluidic device.

Chemicals and Materials	Vendor
Trichlorosilane	Sigma-Aldrich
Polydimethylsiloxane (PDMS)	The DOW Chemical Company
Microscope glass slides	VWR International

Table 5.2: Equipment used in making droplet-based microfluidic device.

Equipment	Equipment name	Brand
Desiccator/Pump	Vacuumcontroller	KnF
Sonicator	2510 Ultrasonic Cleaner	Branson
Spincoater	Polos 300 spin coater	Spincoating
Oven	-	Binder

5.1.1. HYDROPHOBIZATION

3D printed molds were hydrophobized using Trichlorosilane. The reason for doing this is to make peeling the PDMS off the mold easier. Before starting, the molds were cleaned with methanol and dried with compressed air. The molds were then placed inside a desiccator where 3 drops (10 μ l each) of Trichlorosilane was added on a glass petri dish using a micropipette. A pump was connected to the desiccator and depressurized to 100 mbar. The desiccator containing the molds was then set aside for up to 3 hours. When hydrophobization was complete, the molds were wiped clean with methanol and dried. The 3D printed molds were used for a maximum of 4 times in making PDMS molds.

5.1.2. POLYDIMETHYLSILOXANE (PDMS) MOLDING

In this process, PDMS mold was obtained by way of casting. Prior to this, PDMS and the curing agent were mixed in a 50 ml self-standing test tube, at a weight ratio of 7:1 respectively. Using a metal ladle the mixture was mixed until it turned semi-translucent. The test tube was then placed inside a centrifuge. The mixture was centrifuged at 7400 rpm for 15 minutes in order to cause air bubbles and dust particles to settle at the bottom of the test tube. A mold was placed in a glass petri dish where the mixture was poured over it until it was submerged. Air bubbles found in between the 3D printed mold and glass petri dish, during pouring of PDMS over mold needed to be removed. Hence, the petri dish was placed inside a desiccator and depressurized to 100 mbar and set aside for about 30 minutes. The pressure within the desiccator was slowly removed by opening the valve. By so doing, all air bubbles were completely removed. The glass petri dish was then placed in a 90°C oven for 20 to 30 minutes to cure the PDMS. An oven temperature of 65°C over a 12 hour period could also be used. Once curing was complete, the PDMS was cut and easily peeled off the mold. In this case, the PDMS mold had the same dimensions as the 3D printed mold as shown in figure 5.3. Prior to bonding, the inlet and outlet tubing holes were cored into the molded circles using a blunt tip needle. The PDMS mold was also reduced to dimensions of 34 mm length and 24 mm width in order to get rid of bent edges that may affect the bonding process.

5.1.3. SPIN COATING

This process involved uniformly spreading PDMS over a glass slide. To do this, glass slides were wiped clean with methanol and then dried to get rid of dust particles. PDMS and curing agent in this case, were rather mixed at a weight ratio of 10:1 respectively. The mixture was mixed until it turned semi-translucent. Air bubbles and dust particles were caused to settle at the bottom of a test tube by centrifuging the mixture at 7400 rpm for 15 minutes. About 0.5 ml of the mixture was carefully poured on a glass slide using a 1 ml syringe, which was then placed in a desiccator to remove air bubbles. The glass slide was then placed in a spin coater to uniformly spread the PDMS over the glass slide as shown in figure 5.1

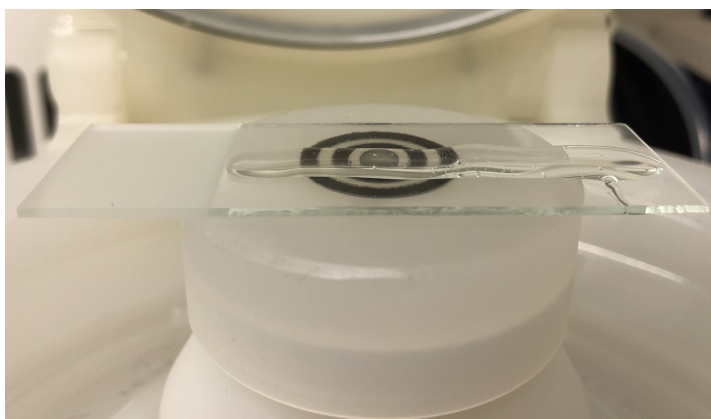


Figure 5.1: PDMS on a glass slide in a spincoater.

5.1.4. SEMICURING AND BONDING

Once the spin coating is complete, the glass slide was then placed in a 65 °C oven for 16-22 minutes depending on the amount of PDMS (0.5-1.0 ml) on glass slide. Extreme care was taken to avoid over-curing and under-curing. The semi-curing has to be done such that the PDMS becomes sticky and leaves no wet mark on the

finger when touched. Under-curing will lead to PDMS seeping into the channels as well as the inlet and outlet tubing holes. Bonding will be impossible when the PDMS is over cured. The molded PDMS was then carefully placed on the semi cured PDMS glass slide. Since the PDMS mold may not be entirely flat, another glass slide and a piece of tissue paper was placed on top of it and taped together to form a sandwich as seen in figure 5.2. The PDMS-glass slide sandwich was then placed in an oven at 65 °C for 12 hours or overnight.

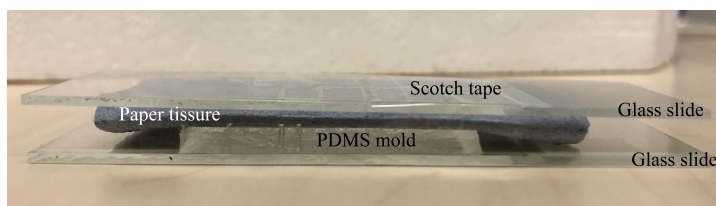


Figure 5.2: PDMS-glass slide bonding process.

5.2. RESULTS AND DISCUSSIONS

The 3D printed mold designed by Tsun Wang Yu (a previous mater student) [9] was used for the production of microfluidic devices. As explained, due to the movement of droplets in straight channels, chambers were rather introduced as part of the channels to help impose some restrictions on the droplets. The dimensions of the chamber were 200 μm high, 400 μm wide, and 1200 μm long. The entire dimensions for the 3D printed mold were 27 mm wide, 40 mm long, and 3 mm thick as shown is figure 5.3.

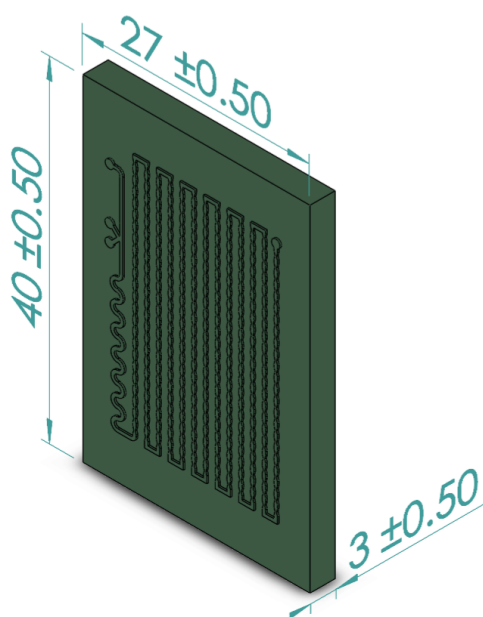


Figure 5.3: Droplet-based 3D printed mold designed by Tsun [9].

The droplets formed were basically made of the dispersed phase engulfed in the continuous phase. The two streams of the dispersed phase mix together at the K-junction where the continuous phase then splits it into droplets. Based on dimensionless numbers (i.e. Reynolds, Bond, capillary and Weber numbers) calculated by Tsun [9], it was realized that the interfacial forces dominated all other forces which led to stable size monodisperse droplets.

These droplets then go through the bending section of the device where complete internal mixing is enhanced. The droplets were then stored in the chambers for a maximum experimental period of 5 hours. The process of droplet formation, internal mixing, and storing is shown in figure 5.4.

As droplets are stored in these chamber they will take an ellipsoidal shape with the volume = $4/3 \times \pi \times a \times b \times c$, where a, b are half the size of the chamber height and width respectively. The length of the droplet however

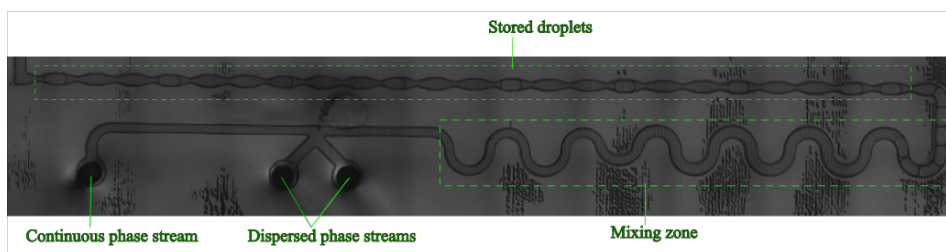


Figure 5.4: Microscope image of device showing droplet formation, internal mixing, and storage. Scale bar = $100\mu\text{m}$

will vary depending on the flow rate of the continuous phase and will not be the same as half the size of the chamber length. The volume of each droplet produced during the experiments was roughly $0.035\ \mu\text{L}$

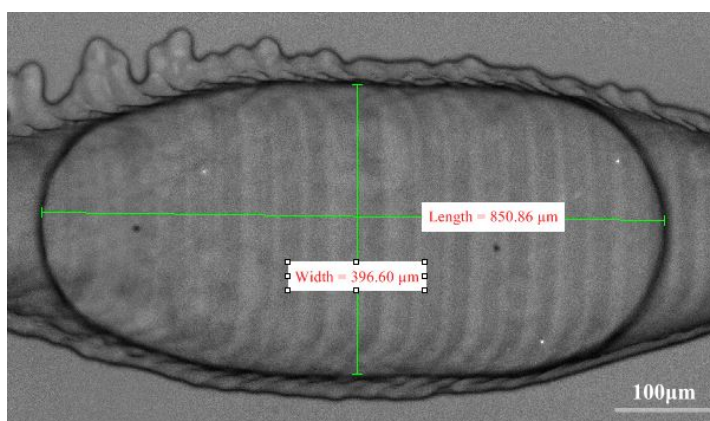


Figure 5.5: Dimensions of a microfluidic droplet. width = $396.60\ \mu\text{m}$ and length = $850.86\ \mu\text{m}$

Several things could go wrong during the production and usage of the microfluidic device. The most important things considered before proceeding to the induction time measurements were as follows:

- The diameter of hole at the top of the PDMS mold from which the tubes are inserted should be smaller than the hole where the fluid leaves into the channels. This was done by placing the PDMS mold on a hard surface and then drilling the holes. Creating an uneven hole diameter at both sides of the PDMS mold will ensure that the tubing are held tightly in place and prevent any pressure and fluid leakages.
- The avoidance of dust in the device channels is also crucial to flow and droplet formation. Aside causing heterogeneous nucleation, dust in channels could split some droplets into smaller droplets creating a large variation in droplet sizes which in the end will influence the nucleation rate. This means that larger droplets will contain many crystals whereas smaller droplets will contain few or single crystals, all within one experiment.
- After the final pressure was chosen, an appropriate amount of time was allowed before stopping the flow. This was to allow the system to reach a steady state flow at the inlets and to ensure a stable emulsification process.

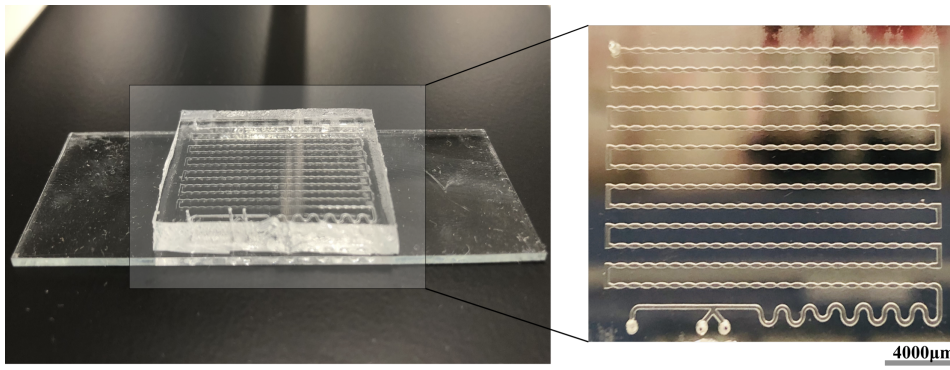


Figure 5.6: A complete droplet-based microfluidic device highlighting the channels, three inlets, and one outlet port.

6

MICROFLUIDIC CRYSTALLIZATION

6.1. EXPERIMENTAL SETUP AND PROCEDURE

The experimental setup consisted of a reservoir, microfluidic device, Nikon inverted microscope equipped with the NIS-Elements imaging software, and a pressure pump which was controlled by Fluigent's All-in-One (AiO) software. For induction time measurements, polarizing filters were used in conjunction with a motorized XY microscope stage that provided a supporting platform for the microfluidic device. Half the area of the microfluidic device was used under 10x objective lens in order to optimize the time lapse imaging process.

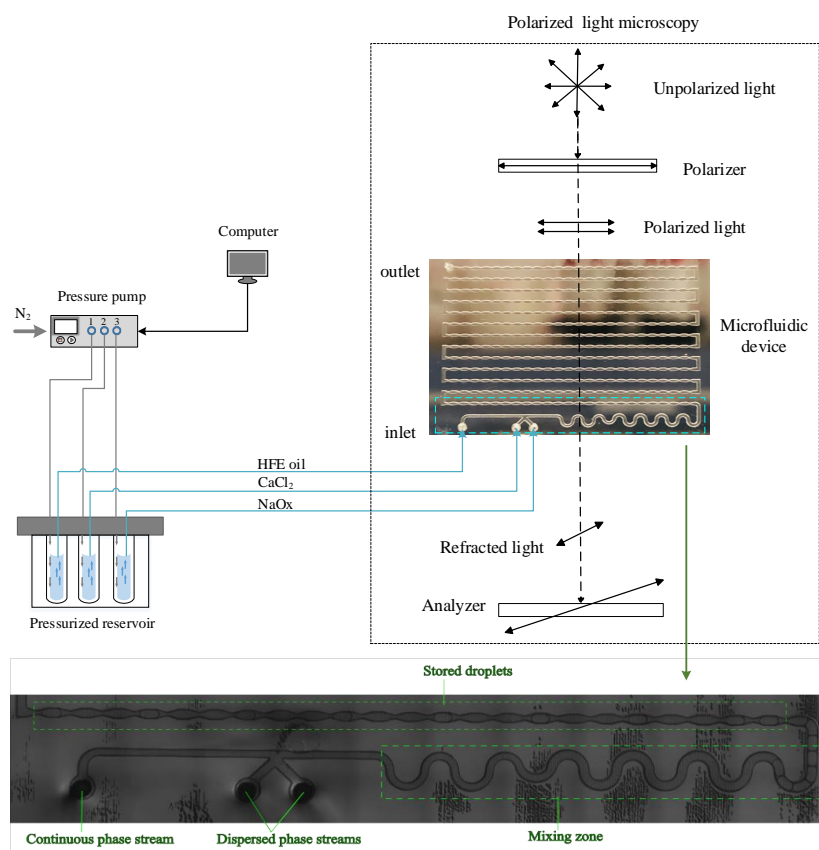


Figure 6.1: Microfluidic crystallization experiment setup for induction time measurements.

6.2. MATERIALS AND METHODS

Table 6.1: Equipment used during microfluidic crystallization experiments.

Equipment	Equipment Name	Brand
Pressure pump	MFCS - EZ	Fluigent
Microscope	Ti-eclipse	Nikon
Scale	-	Mettler Toledo
Sonicator	2510 Ultrasonic Cleaner	Branson
Heating plate	-	iSL

Table 6.2: Chemicals needed for microfluidic crystallization experiments

Compound name	Chemical formula	Vendor
Sodium chloride	NaCl	Fluka
Potassium chloride	KCl	Emsure
Ammonium chloride	NH ₄ Cl	Sigma-Aldrich
Creatinine	C ₄ H ₇ N ₃ O	Sigma-Aldrich
Urea	CH ₄ N ₂ O	Emprove
Tri-sodium citrate	Na ₃ C ₆ H ₅ O ₇	Emprove
Magnesium sulfate heptahydrate	MgSO ₄ · 7H ₂ O	Sigma-Aldrich
Sodium sulphate	Na ₂ SO ₄	Sigma-Aldrich
Sodium phosphate monobasic	NaH ₂ PO ₄	Sigma-Aldrich
Calcium chloride	CaCl ₂	Sigma-Aldrich
Sodium oxalate	Na ₂ C ₂ O ₄	Sigma-Aldrich
Hydrofluoroether (HFE)	3-Ethoxy-1,1,1,2,3,4,4,5,5,6,6,6-dodecafluoro-2-trifluoromethylhexane	3M
Pico-Surf 1	-	Sphere Fluidics
Ultra pure water	H ₂ O	Elga
Hyaluronic acid	(C ₁₄ H ₂₁ NO ₁₁) _n	Sigma-Aldrich

6.2.1. PREPARATION OF DISPERSED PHASE AT DIFFERENT OXALATE CONCENTRATION

The dispersed phase consists of a mixture of calcium chloride and sodium oxalate streams as shown in the experimental setup above. A constant calcium chloride concentration was used while varying sodium oxalate concentration. In order to prepare the solutions for these two inlet streams, the amount of calcium chloride and sodium oxalate used are indicated in table 6.3. These amounts were each dissolved in 10 ml artificial urine and were protected against any dusts. The dissolution was done at room temperature with a magnetic stirrer at 300 rpm for 15 minutes on a heating plate. The preparation of artificial urine was the same as mentioned in section 3.3.1. Prior to usage, both calcium chloride and sodium oxalate solutions were filtered through 0.45 μm pore filters.

Table 6.3: Amount chemicals required to prepare the dispersed phase

Compound	Initial concentration (mM)	Amount in mg/10ml artificial urine
Calcium chloride	12	13.32
Sodium oxalate	1.0	1.34
	1.7	2.28
	2.4	3.22

¹ The final concentrations of calcium chloride and sodium oxalate in droplets will be half of the initial concentrations

6.2.2. PREPARATION OF DISPERSED PHASE AT DIFFERENT HA CONCENTRATIONS

The same method of as described in section 6.2.1 above was used for preparing the calcium chloride solution. The difference here is the presence of Hyaluronic acid in the sodium oxalate solution. The amount of sodium oxalate and hyaluronic acid were dissolved in 10 ml artificial urine. Due to the presence of hyaluronic acid, the dissolution was done with a magnetic stirrer at 700 rpm for 45 minutes on a heating plate at room temperature. Prior to usage, both calcium chloride and sodium oxalate - HA solutions were filtered through 0.45 μm pore filters.

Table 6.4: Amount chemical required to prepare dispersed phase at different HA levels

Compound	Initial concentration [mM]	Amount in mg/10ml artificial urine
Calcium chloride	12	13.32
Sodium oxalate	1.7	2.28
Hyaluronic acid	0.001	0.69
	0.007	5.0
	0.014	10.0

6.2.3. PREPARATION OF CONTINUOUS PHASE

HFE oil was used due to its compatibility with PDMS where no diffusion occurred. The introduction of surfactant was very necessary in order to reduce surface tension. The continuous phase was prepared by mixing HFE oil with 0.5% V/V pico surfactant. A new amount of continuous phase was always prepared for each and every experiment.

6.2.4. MICROFLUIDIC CHIP INJECTION

The pressure pump works such that the nitrogen gas through the pressure controller pressurizes the reservoir (Eppendorf tubes) by pushing on the fluid surface causing it to flow out of the reservoir outlet to the inlet of the microfluidic chip. Based on resistance experienced in the tubes the pressure controller readjust the pressure to ensure uniform and equal flow rates in all connecting tubes.

Prior to the start of the pressure pump, the calcium chloride and sodium oxalate solutions were filtered using 0.45 μm pore filter. The solutions were then injected into separate Eppendorf tubes using 5 ml syringes. The same was done for the HFE oil except the filtration part. Injection of fluid into the reservoir through the connecting tubes gets rid of air and air droplets that imposes enormous restrictions on the fluid flow and cause backflows. Once each reservoir was filled with about 1.5 ml of solutions, the pressure valve was opened and the pressure divider turned on. The pressure pump was then started using the play button at the front bottom left part of the pump. The tubes connecting the pump to the reservoir and the reservoir to the microfluidic device were all connected. The droplet generation was then began by slowly increasing the pressure using the Fluigent AiO software. A final pressure of 75 mbar was used for both the calcium chloride and sodium oxalate streams, while 74.8 mbar was used for the HFE oil-surfactant stream. The same injection method was also used for the experiment where sodium oxalate solution contained HA.

6.2.5. POLARIZED LIGHT MICROSCOPY

As seen previously, using crossed polarized light only highlights COM crystals while rendering COD crystals invisible. The aim is to highlight both crystals in order to study their induction time. To be able to overcome this, polarized light was combined with white light at the same time. By so doing, the polarized light highlighted the COM crystal, while the white light highlighted the COD crystals. This method provided a very unique way of identifying both crystals in a microreactor for the first time.

In the experimental set up, an oblique angle of 20° for the polarizer was used throughout the microfluidic. With this angle, a portion of white light became polarized while a portion went through the polarizer without any refraction. The method of setting up the polarizer for the experiment is described as follows:

1. A sample image of the chip using 10x objective lens is taken to ensure the center of the chip is well positioned.
2. The polarizer is placed in the path of white light.

3. The polarizer is rotated clockwise until the calibrations on the polarizer holder coincides with the 20° angle.
4. The light intensity is set to a suitable level, 3.0 was usually used.
5. From the filters tab in the 'NIS' software, the analyzer option is chosen.
6. The sample usually appears dark after switching to the analyzer, hence the 'LUTS' bars are used to change the contrast.
7. Exposure time is set to 10ms and laboratory lights turned off.
8. The pressure pump is switched off and the experiment is started by taking time lapse images.
9. The connecting tubes to the reservoir are disconnected to ensure droplets remain stationary.

6.2.6. INDUCTION TIME MEASUREMENT

This was the last stage of the experiment where all methods and processes come into play. After droplets were formed and the polarized light microscopy was set up, the induction time measurements was ready to begin. The movement of the motorized XY stage helps the camera to take time lapse images of each channel where the software then stitches them together to create a large image of the specific area selected. The selected area of the microfluidic device under 10x object lens was 17 mm by 12 mm, which was half the original size of the PDMS mold/chip. The large images of this area were taken every 2 minutes which was mostly over a 5 hour period. Obviously each channel contains droplets and while images are taken at time intervals, COM and COD are observed as black and white spots in droplet as seen in the figures 6.2 and 6.4. It can be seen that droplets at 6 and 10 min only showed COD (black spots). Only afterwards did COM (white spots) start to appear. COD which is metastable at room temperature always appeared before the thermodynamically stable COM. This allowed us to distinguish the induction of COD from COM as will be seen in section 6.3.

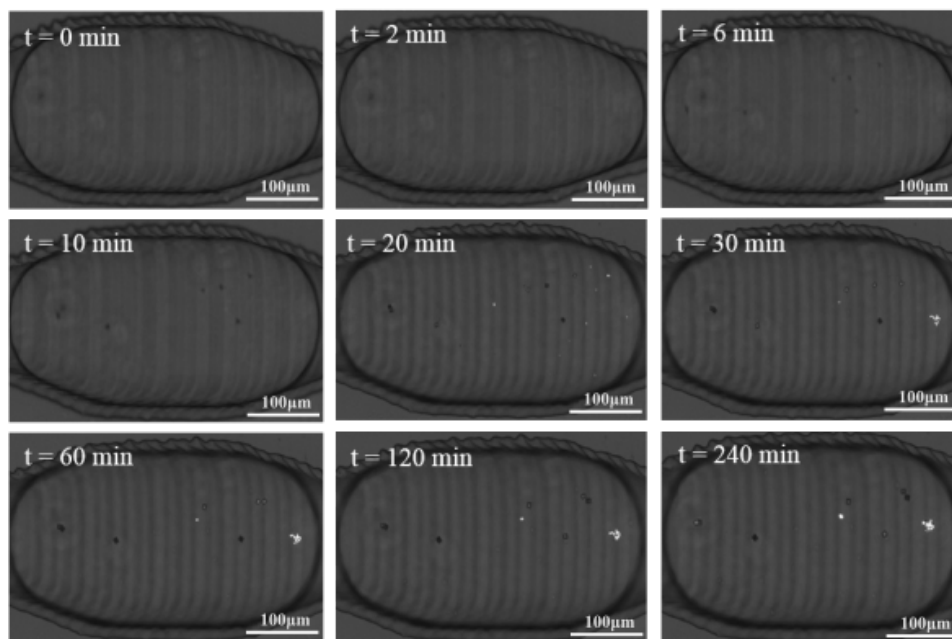


Figure 6.2: Time lapse images of COM and COD (at $[Ca]=6.0mM$, $[Ox]=1.2mM$) using polarized light microscopy

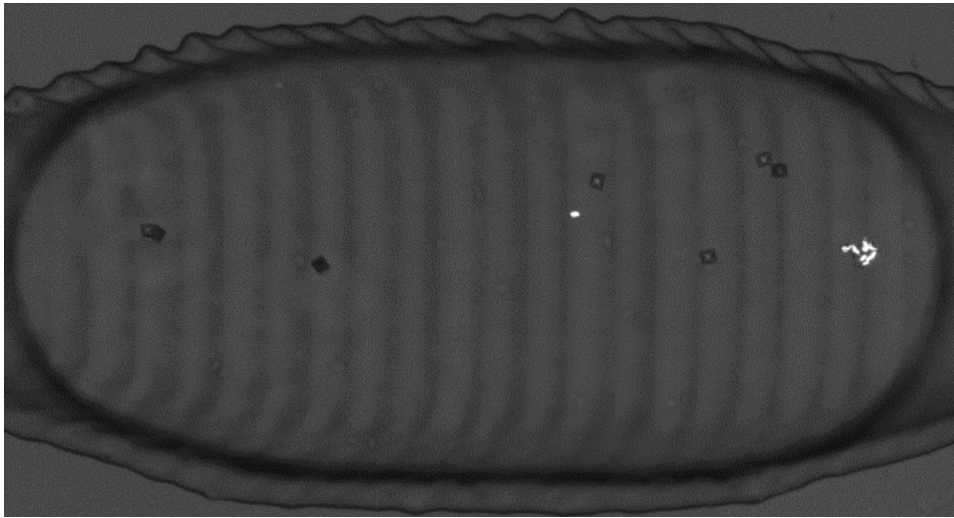


Figure 6.3: Image of a droplet highlighting COM (white) and COD (black) with the use of polarized light microscopy at time $t=240\text{min}$, polarizer angle = 20° , and scale bar = $100\mu\text{m}$

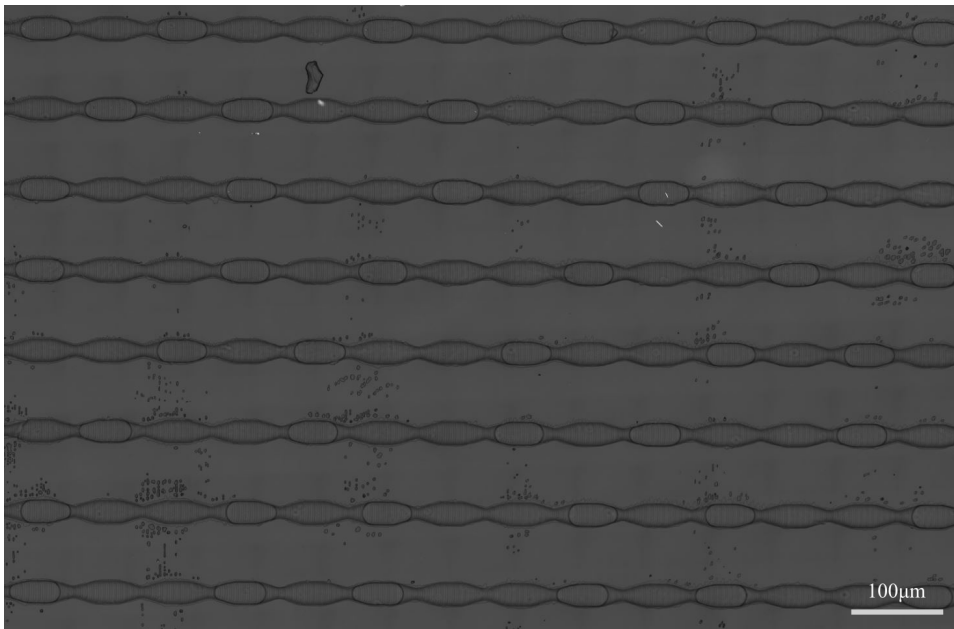


Figure 6.4: A large image of the microfluidic device as per the specified area (17×12) using 10x objective lens

6.3. RESULTS AND DISCUSSIONS

The effect of varying oxalate as well as hyaluronic acid concentrations on the induction time of COM and COD was successfully examined. In all cases, the concentration of calcium chloride, thus 6.0mM, was kept constant during the preparation of solutions. Induction time measurements were always performed at constant room temperature.

Consistency in results was very important, hence conditions that could be controlled were always the same. For instance, pressure applied to the inlet streams were the same for each experiment. It was very important to ensure the same pressure as it influences droplets size. Furthermore, experiment for each condition was repeated twice in order to get the average nucleation probability and induction time. The number of droplets analysed for each experiment set were within the range of 50 to 90.

In terms of microscopy, light intensity level of 3.0, polarizer angle of 20°, and 10x objective lens were used throughout the experiments. At these settings and with a specified area of 17 mm by 12 mm, it took approximately 1.5 minutes to capture a large of the microfluidic device. Although, these images were only displayed after 2 minutes. This time was very crucial in selecting the concentration of calcium chloride and sodium oxalate. The precipitation must not be too fast as nucleation will be missed before the image is captured. As CaOx can exist in more than one crystalline form, it was important to monitor the experiment for a longer time.

CALCIUM OXALATE IN DROPLETS

During the nucleation of calcium oxalate, it was realized that all droplets contained COM. But some of these droplets also contained COD at the same time as shown in figure 6.5. It was important to point this out in order to understand if the induction time of COM may perhaps vary in both the presence and absence of COD. The presence of COD can act as a template thereby promoting the crystallization of a different type of crystal, thus COM, through secondary nucleation.

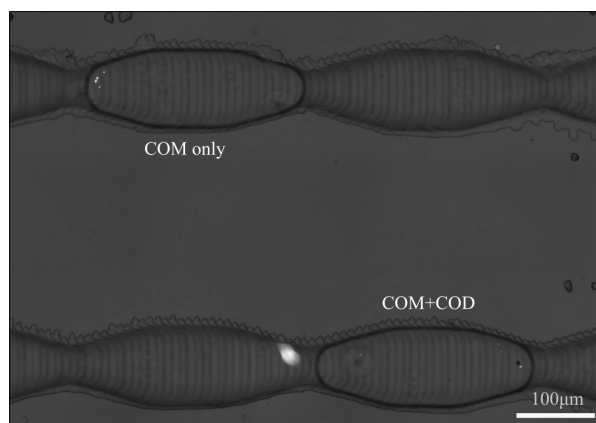


Figure 6.5: Image of droplets containing COM only or COM and COD

6.3.1. INDUCTION TIME OF CALCIUM OXALATE AT DIFFERENT OXALATE CONCENTRATIONS

As always mentioned, 6.0mM of calcium chloride concentration was used throughout the experiments. In contrast, sodium oxalate concentration was varied to create different supersaturations. In figure 6.6, the cumulative probability of COM and COD was plotted against detection time. The Weibull model was then fitted to the experimental data.

As can be seen, the COM probability is 1 at the three different conditions. COD however, was not always found in all the droplets making its probability less than 1. The detection time for COD was also shorter at high levels of sodium oxalate compared to COM. The appearance of COD in figure 6.6a and 6.6b happened just after 2 minutes from the start of experiment, while COM started to form after 4 minutes. Whereas in figure 6.6c where oxalate concentration was much lower, COD started to form after 6 minutes while COM formed after 10 minutes. At all conditions COD always formed before COM and this will be seen when from the median induction times are calculated.

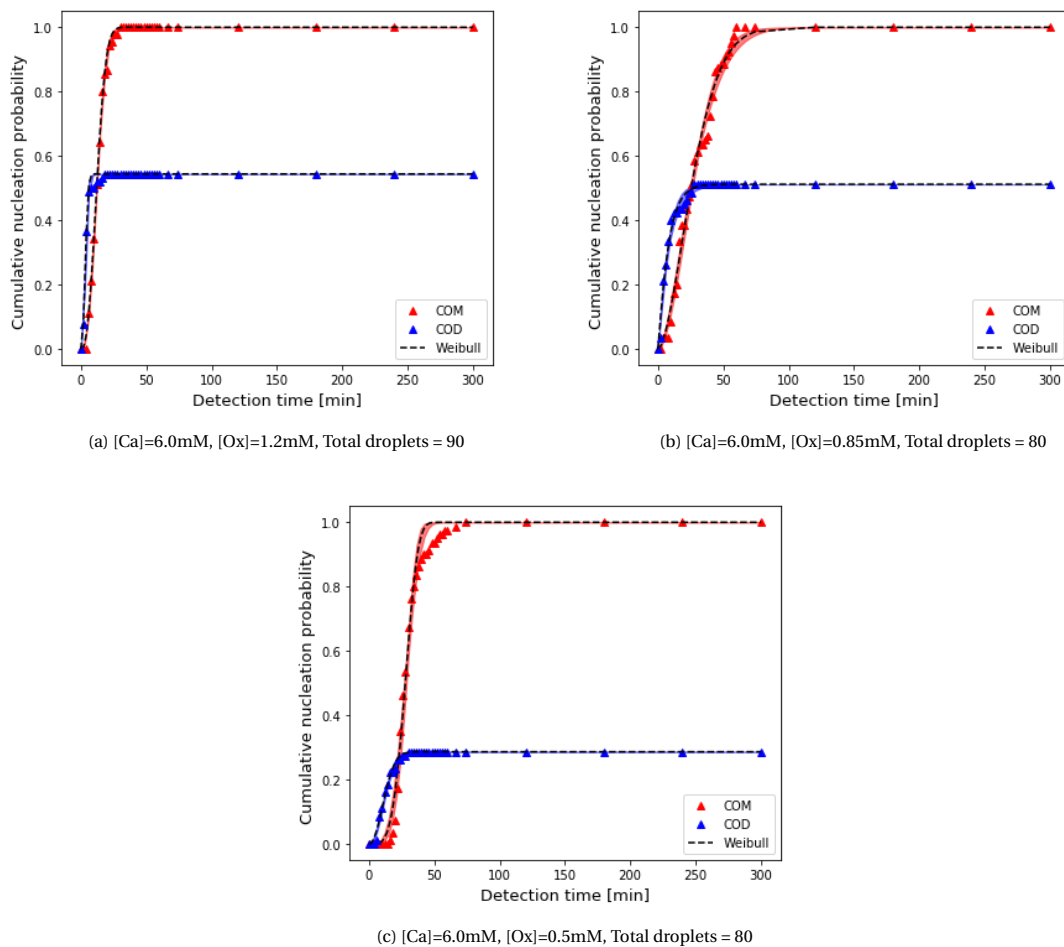


Figure 6.6: Individual probability curves of COM vs COD at different oxalate concentrations

EFFECT OF OXALATE ON COM INDUCTION TIME

In order to see how probability curves of COM vary as oxalate concentration is decreased, the COM plots in figure 6.6 were combined as shown in figure 6.7. It is as expected that the detection time will decrease as oxalate levels dropped. The nucleation of COM at $[Ox] = 0.5 \text{ mM}$ was very long at it took about 16 minutes for COM to be observed and 72 minutes for all the droplets to contain COM. Although COM at $[Ox] = 0.85 \text{ mM}$ was fast in nucleating, it took about 60 minutes for all the droplets to contain COM. The COM at $[Ox] = 1.2 \text{ mM}$ was the fast at nucleating and was also found in all droplets in just 30 minutes. Clearly, a decrease in oxalate concentration made detection time longer.

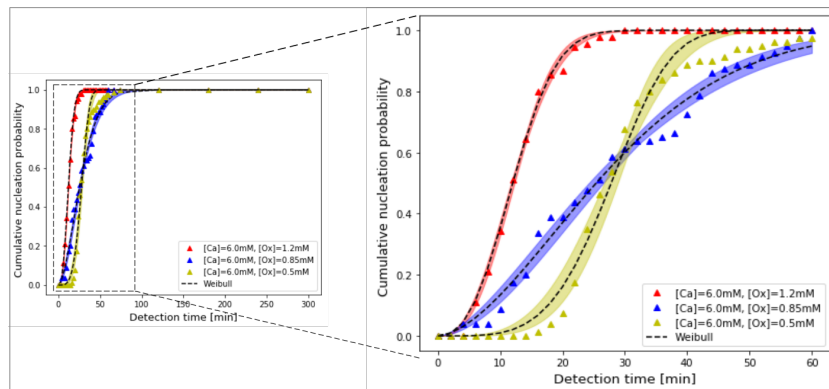


Figure 6.7: Combined probability curves for COM at different oxalate concentrations

Also, it is expected that the nucleation rate J , will increase with increasing HA concentrations. However, in order to get more insight about nucleation, numerical parameters for COM from the model such as τ and k values needed and are shown in table 6.9. The time scale τ is basically a parameter that relates to the median induction time, t_{MED} , as given in equation 2.29. The k parameter on the other hand gives information about an increasing or decreasing nucleation. When $k > 1$, the nucleation rate increases with time. But when $k < 1$, the nucleation rate decreases with time. Also, larger k values signify a longer initial plateau at the start of nucleation [49].

As seen in table 6.5, the oxalate concentration decreased, the time scale τ increased. Large k values at $[Ox] = 0.50$ mM indicated a longer plateau at the beginning of nucleation as seen in figure 6.7.

Table 6.5: τ and k parameters for COM obtained from the fitted Weibull model at different oxalate concentration

Calcium (mM)	Oxalate (mM)	τ (min)	95% confidence interval	k	95% confidence interval
6.0	1.20	13.91	13.71, 14.11	2.51	2.38, 2.64
	0.85	31.52	30.68, 32.37	1.70	1.58, 1.82
	0.50	30.37	29.64, 31.10	4.17	3.63, 4.73

Using τ and k values to calculate t_{MED} , showed a decreasing median nucleation time as oxalate concentration decreased. This meant that nucleation rate, J will decrease which was what was seen in table 6.6

Table 6.6: Median nucleation time and nucleation rate of COM at different oxalate concentration

Calcium (mM)	Oxalate (mM)	t_{MED}	$J(nuclei\ s^{-1}\ L^{-1})$
6.0	1.20	16.10	29582.67
	0.85	39.15	12162.09
	0.5	33.16	14360.33

EFFECT OF OXALATE ON COD INDUCTION TIME

As was the case for COM, all COD probability plots in 6.6 were combined as shown in figure 6.8. The detection time for COD at $[Ox] = 1.2$ mM was the shortest, while that at $[Ox] = 0.5$ mM was the longest. This was expected as decreasing oxalate concentration meant a decrease in driving force for nucleation to occur.

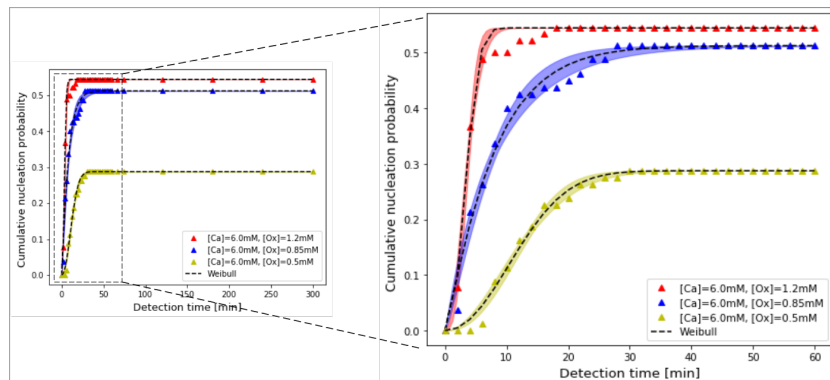


Figure 6.8: Combined probability curves for COD at different oxalate concentrations

Similar to COM, decreasing oxalate concentration led to an increase in the time scale, τ . Combining it with the k values, led to an increase in the median nucleation times and a decrease in the nucleation rate of COD.

Table 6.7: τ and k parameters for COD obtained from the fitted Weibull model at different oxalate concentration

Calcium (mM)	Oxalate (mM)	τ (min)	95% confidence interval	k	95% confidence interval
6.0	1.20	3.98	3.81, 4.16	2.37	2.03, 2.71
	0.85	8.08	7.58, 8.57	1.10	0.98, 1.21
	0.50	14.04	13.6, 14.48	2.11	1.91, 2.30

Table 6.8: Median nucleation time and nucleation rate of COD at different oxalate concentration

Calcium (mM)	Oxalate (mM)	t_{MED}	$J(nuclei\ s^{-1}L^{-1})$
6.0	1.20	4.65	102502.72
	0.85	11.27	42234.29
	0.50	16.70	28508.57

INFLUENCE OF COD ON COM INDUCTION TIME AT VARYING OXALATE CONCENTRATIONS

Figure 6.9 is basically a subsection of the COM plots which shows how the detection time of COM will vary in the presence and absence of COD. In figure 6.9a, the probability curves basically overlapped each other will. However, in figure 6.9b the detection for COM in absence of COD (blue) was shorter compared to when COD was present (red). The opposite was rather seen in figure 6.9c. As will be seen in other results, the COD seem to have no significant effect on COM detection time.

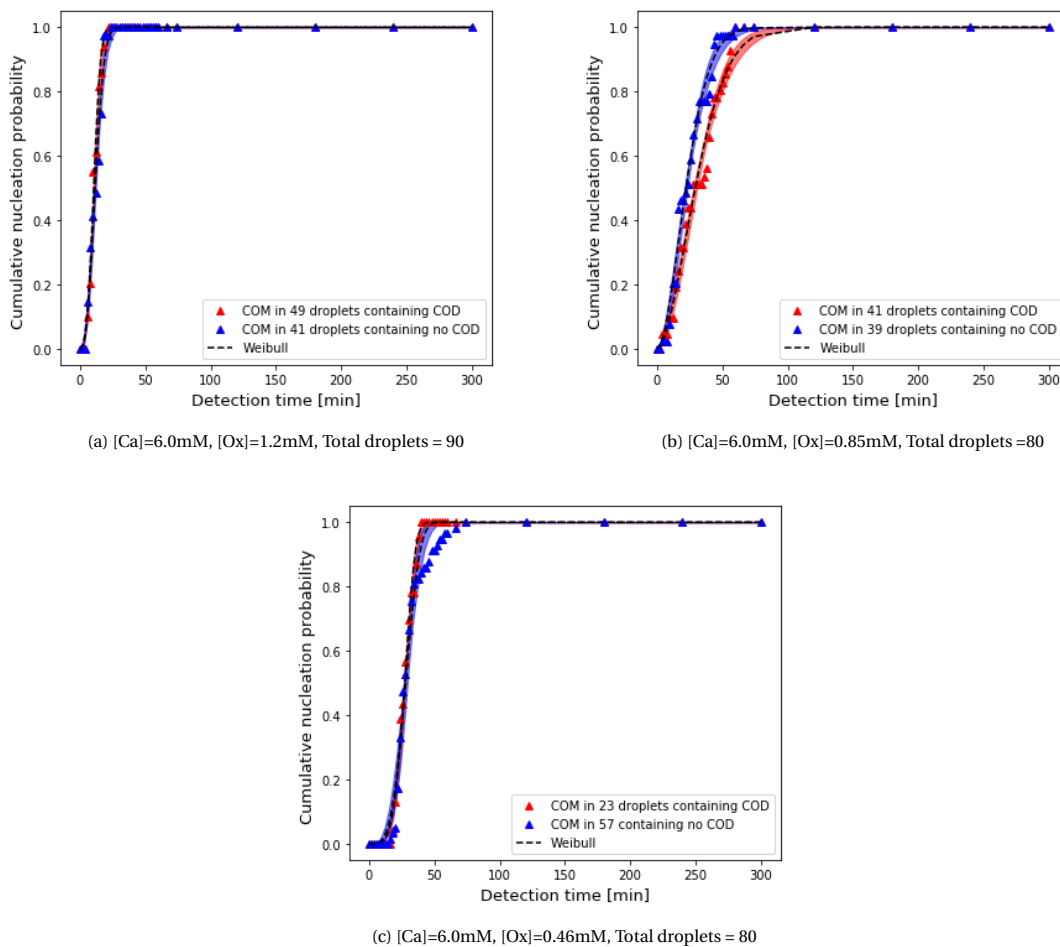


Figure 6.9: Effect of COD on COM induction time at different oxalate concentration

6.3.2. INDUCTION TIME OF CALCIUM OXALATE AT DIFFERENT HA LEVELS

Based on the experimental results obtained section 6.3.1, the control group was defined by using 6.0 mM of calcium chloride and 0.85 mM of sodium oxalate, while varying amount of HA, as was shown in table 6.4. This means that droplets generated contained calcium and oxalate ions as well as hyaluronic acid. In figure 6.10, the cumulative probability was plotted against detection time for each HA concentration. The Weibull model (dotted black lines) was also fitted with all the experimental data points.

Similar results in terms of the cumulative probability for COM and COD in the presence of HA (figure 6.10) can be seen when compared with probabilities in the absence of HA as seen previously (figure 6.6). Irrespective of the total droplets per experiment, the probability of COM was always 1 indicating that all droplets contained COM. On the other hand, the probability of COD was always less than 1, indicating that only a fraction of the droplets contained COD. Regarding curve fitting, the Weibull model was able to predict the experimental data perfectly.

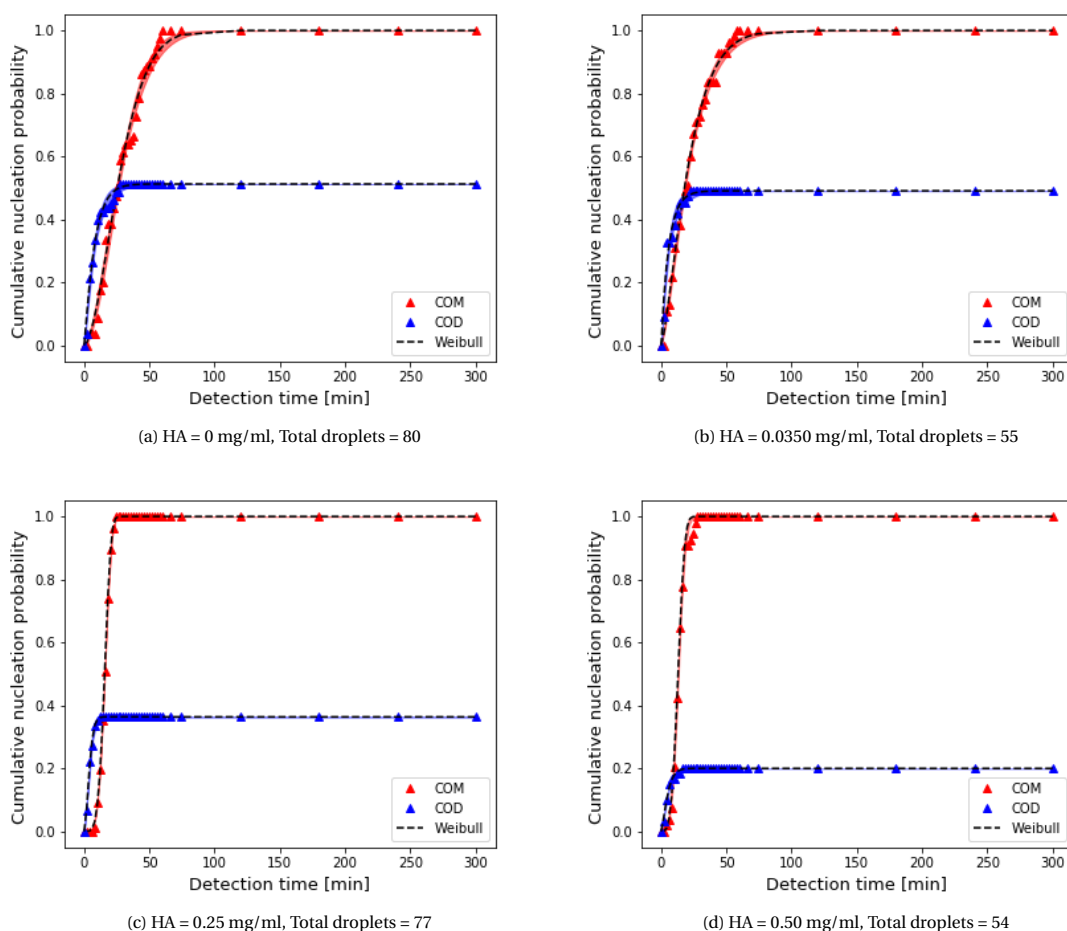


Figure 6.10: Individual probability curves of COM vs COD at different HA concentrations

EFFECT OF HA ON COM INDUCTION TIME

In order to clearly see and compare the effect of HA, the individual COM and COD curves in 6.10 were combined into one plot, as seen in figure 6.11 and figure 6.12. In figure 6.11, the detection time was shorter as HA concentration increased. This means that COM crystals appeared much faster in droplets containing the highest concentration of HA.

As shown in table 6.9, k increases with decreasing τ as HA increase. This means that the nucleation rate

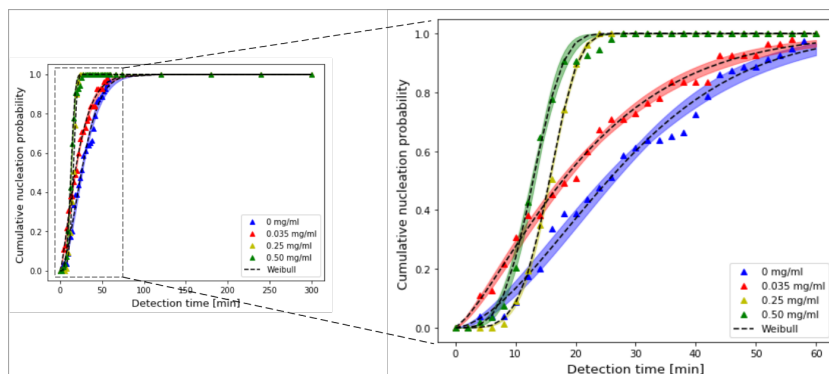


Figure 6.11: Combined probability curves for COM at different HA concentrations

of COM will also increase with time. Since k values at HA concentration of 0.25 mg/ml and 0.5 mg/ml were large, it made sense that they will have a longer plateau at the on beginning of nucleation.

Table 6.9: τ and k parameters for COM obtained from the fitted Weibull model at different HA concentration

Hyaluronic acid (mg/ml)	τ (min)	95% confidence interval	k	95% confidence interval
0	31.52	30.68, 32.37	1.69	1.58, 1.82
0.035	23.51	22.94, 24.08	1.32	1.26, 1.39
0.25	16.94	16.86, 17.02	4.63	4.50, 4.76
0.5	14.28	14.04, 14.52	3.68	3.37, 3.99

Based on the droplets volume, the nucleation rates of COM at different HA concentrations were calculated and presented in table 6.10. It can be seen that as HA increased, the nucleation rate of COM increased with a decreasing median nucleation time. This promotory effect of HA on nucleation rate was also observed by Poon [28] where they considered CaOx as a whole. The fascinating part of this work was that individual CaOx hydrates could be distinguished instead of considering them as a whole.

Table 6.10: Median nucleation time and nucleation rate of COM at different HA concentration

Hyaluronic acid (mg/ml)	t_{MED} (min)	J ($nuclei\ s^{-1}\ L^{-1}$)
0	39.15	12162.09
0.035	31.03	15344.10
0.25	18.34	25970.98
0.5	15.78	30185.51

EFFECT OF HA ON COD INDUCTION TIME

In the case of COD, a rather contradicting effect of HA was seen. HA acted as an inhibitor as can be seen in figure 6.12. The detection time became longer at HA concentration of 0.50 mg/ml as compared to 0 mg/ml, 0.035 mg/ml and 0.25 mg/ml. This means that the appearance of COD in droplets was slower at high HA.

The τ and k parameters for COD were also presented in table 6.11. The k values at HA concentrations of 0 mg/ml and 0.035 mg/ml had lower limit confidence intervals less than 1, all others were above but very much close to 1. Low values of k at all conditions showed a non-existing plateau at the beginning of nucleation. The τ values also became smaller as HA was introduced in droplets.

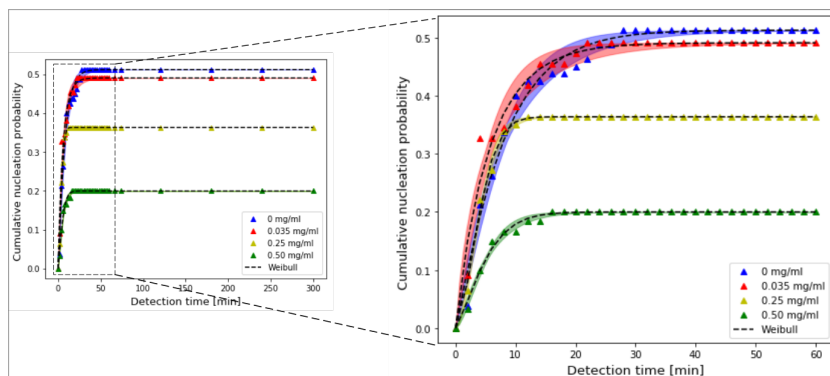


Figure 6.12: Combined probability curves for COD at different HA concentrations

Table 6.11: τ and k parameters for COD obtained from the fitted Weibull model at different HA concentrations

Hyaluronic acid (mg/ml)	τ (min)	95% confidence interval	k	95% confidence interval
0	8.07	7.58, 8.57	1.1	0.98, 1.21
0.035	5.70	5.17, 6.23	0.97	0.84, 1.10
0.25	4.59	4.45, 4.72	1.68	1.56, 1.80
0.5	5.43	5.17, 5.69	1.34	1.21, 1.47

From calculations, the median nucleation time and nucleation rate showed fluctuating results as shown in table 6.12. Comparison of t_{MED} between 6.10 and 6.12 clearly reiterates the fact that COD indeed did form before COM

Table 6.12: Median nucleation time and nucleation rate of COD at different HA concentration

Hyaluronic acid (mg/ml)	t_{MED}	J (nuclei $s^{-1} L^{-1}$)
0	11.26	42286.63
0.035	8.32	57254.34
0.25	5.71	83410.60
0.5	7.14	66710.46

INFLUENCE OF COD ON COM INDUCTION TIME AT VARYING HA CONCENTRATIONS

As seen in figure 6.13a, the detection time of COM in the presence of COD (red) was slightly longer than that of COM in the absence of COD (blue). On the other hand, the detection time of COM in both the presence and absence of COD were basically overlapping as seen in figure 6.13b, 6.13c, and 6.13d. In general, COD did not have any effect of detection time of COM in droplets.

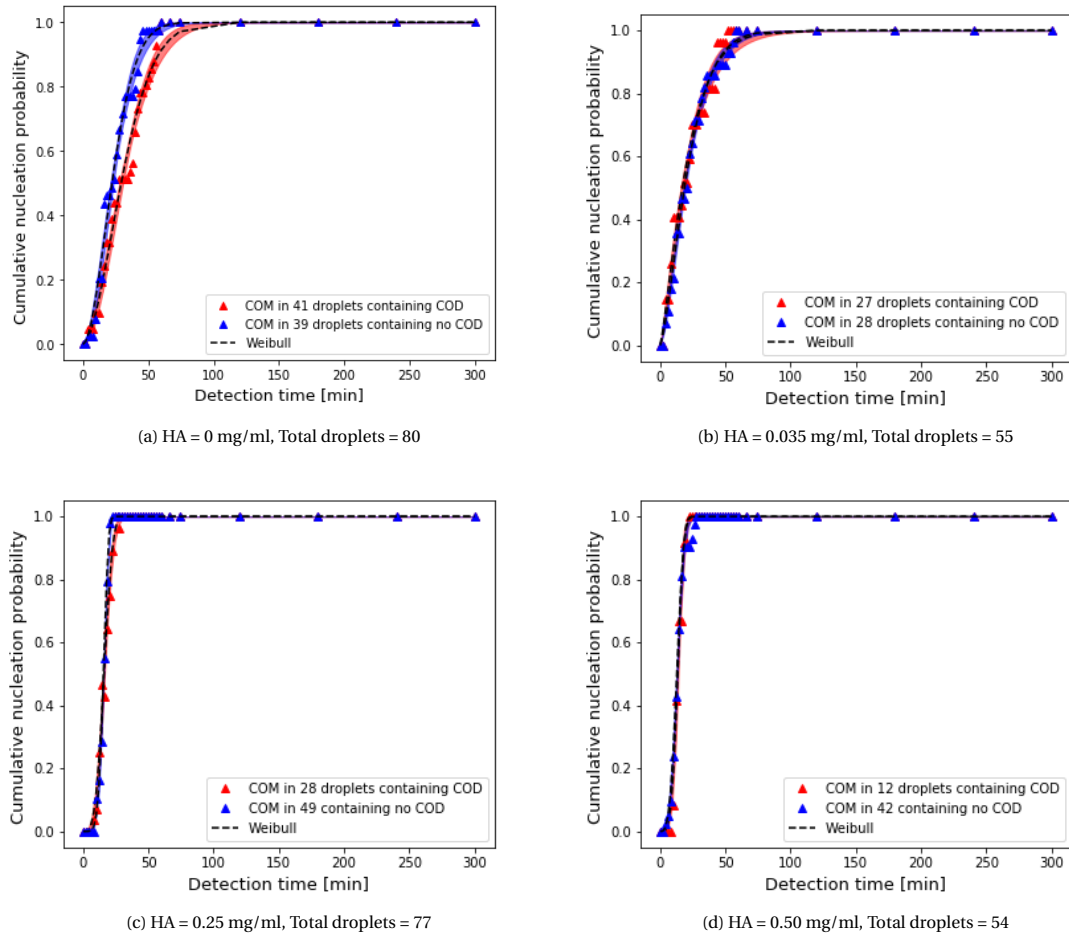


Figure 6.13: Effect of COD on COM detection time at different HA concentrations

7

CONCLUSIONS & RECOMMENDATIONS

7.1. CONCLUSIONS

7.1.1. RAMAN SPECTROSCOPY

Crystallizing a particular compound from artificial urine solution can be very difficult. Due to the large number of different compounds in the artificial urine, several crystal combinations are possible (eg. calcium phosphate, magnesium oxalate, magnesium chloride, magnesium ammonium phosphate, etc.) In order to ensure that the crystals produced are entirely made of calcium and oxalate, Raman spectroscopy was used. The experiments were however carried out in a bulk solution instead of micro-droplets.

The use of equimolar and non-equimolar ratios of the reactants resulted in dominant COM and COD peaks respectively. The peaks obtained in the experiments were identical to those of prominent kidney stone peaks according to literature. The results were also compared with COM powder from a supplier which showed the same peak wavenumbers. Most importantly, a doublet peak which are the main absorption peak for COM were observed at 1463 and 1490 cm^{-1} , and are described by the $\nu(\text{CO})$ stretching mode [55, 56]. On the other hand, the main absorption peak for COD is a singlet peak observed at 1478 cm^{-1} which is assigned the $\nu(\text{CO})$ stretching [57, 58]. Lastly, a less intense peak for COM was observed at 1630 cm^{-1} , and is usually assigned to CO asymmetric stretching mode [58].

The importance of this work relied heavily on the ability of Raman spectroscopy to accurately identify calcium oxalate crystals which usually occur as different hydrates. The base line is, this study revealed only COM and COD in a predominant level.

7.1.2. POLARIZED LIGHT MICROSCOPY

Since a fraction of the droplets always contained both COM and COD, it was very important to identify them at the same time. A polarizer angle of 20° made this possible as both white light and polarized light combined to detect COD and COM respectively. Detecting both hydrates at the same time was a breakthrough moment for the induction time measurements.

7.1.3. INDUCTION TIME MEASUREMENTS

The experiment and analytical methods used allowed for a clear distinction between the induction time of COD and COM. This method of induction time measurements showed how the induction times varied as conditions were changed. The use of the Weibull model also made it possible for the determination of nucleation rates and the median induction times.

The nucleation rates and median induction times were determined using 95% confidence interval. They were determined by fitting a minimum of 50 data points to the Weibull model (Equation 2.30). As was expected, an increase in oxalate concentration meant a possible increase in supersaturation, although supersaturation was not determined. A higher supersaturation, molecules or clusters collide more often and will result in the formation of new crystals within a short time.

The formation of COD before COM could be explained by assuming it has a lower energy barrier. It is however counter intuitive as COD is only found in some droplets and not all droplets. One may also assume that COD in fact did form but later dissolved or transition into COM, at a stage not detectable by the microscope. In short a conclusion could not be drawn on the frequency behaviour of COD in droplets.

Lastly, the frequency of COM was much higher than COD in all the individual droplets. This is exactly what happens in the kidney as more COM is found in clinical stones compared to COD [12].

INFLUENCE OF VARYING OXALATE CONCENTRATION

In all cases, the detection time for COD was shorter than COM indicating that COD did nucleate faster. The probability of COD in droplets never gets to one, meaning that spontaneous crystallization of COD only occurred in some droplets. On the other hand, spontaneous crystallization of COM occurred in all droplets. Lastly, a decrease in oxalate concentration prolonged induction time while decreasing the nucleation rates for both COM and COD.

INFLUENCE OF VARYING HA CONCENTRATION

The presence of HA did not stop COD from forming before COM. The cumulative probability of COD was as usual less than one with COM always having a probability equal to one. The most interesting part was how HA had contradictory effects on COM and COD in terms of induction times. As the concentration of HA increased, it acted as a promoter by shortening the induction time and increasing the nucleation rate for COM. The opposite rather occurred for COD where HA acted as an inhibitor. An increase in HA concentration led to prolonged induction times and slower nucleation rates.

7.2. RECOMMENDATIONS

- **Better understanding of why COD nucleates before COM:** During the induction time measurements, it was clearly seen that COD formed before COM at varying conditions. In order to explain this, thermodynamic parameter (B) and supersaturation (S) should be determined. The nucleation work (W^*) which can be determined by relating it to B and S will describe why nucleation proceeds faster or slower. Also, it will be interesting to know how the kinetic parameter (A) compares with theoretical values.
- **Redefining the induction time for COM:** Induction time is when the first crystal is formed and must be independent of whether the crystal is COD or COM. The basis of the Weibull model is such the appearance of any nucleus must be an independent process. Furthermore, conditions such as supersaturation must remain constant prior to the formation of the first nuclei. Hence, the induction time for COM should only consider droplets containing COM without including those droplets that contain COD and COM. The representation of COD induction time rather captures perfectly the meaning of induction time.
- An explanation for the lower frequency of COD should be derived either theoretically or through experiments.
- The protocol for producing a microfluidic device is very effective except the semicuring part which comes with experience. For every experiment a different chip is used hence, lots of the devices must be produced which is time consuming. A permanent chemically treated microfluidic device with our channel design produced by a company will be very helpful to maintain consistent result and shorten experimental periods.
- Although the use of pressure pump is very reliable, coupling it with a flow sensor to get the desired flow rates of the inlet feed will be much more effective.
- As always, counting crystals manually introduces some degree of errors in the experimental data. Therefore, having a computerized system to that will shorten the time spent for data analysis and also prevent errors.
- The stability of droplets in the channels is very important to keep track of every single droplet. A change in pressure head between the reservoir and the microfluidic device will either cause the droplets to recede into the inlet tubes or proceed out of the chambers through the outlet tube. It is therefore critical to nullify the pressure head by keeping the reservoir and device on the same elevation or height.
- Lastly, the concentration of calcium and oxalate used were within normal range. However, the experiments were carried out at room temperature (Ca. 25°C) which is a huge deviation from normal body temperature (37°C).

Appendices



MATLAB CODE FOR PLOTTING DATA FROM RAMAN EXPERIMENTS

```
1 clear
2 close all
3 filename1 = 'E:\Desktop\kidney stone project\Raman experiments\15-06-20\Artificial
   urine only.xlsx';
4 filename2 = 'E:\Desktop\kidney stone project\Raman experiments\17-06-20\AU from COM
   supplier 1.xlsx';
5 filename3 = 'E:\Desktop\kidney stone project\Raman experiments\17-06-20\AU from CaOx
   .xlsx';
6 filename4 = 'E:\Desktop\kidney stone project\Raman experiments\23-06-20\au from
   4.3-4.3 solution p2.xlsx';
7
8 data1 = xlsread(filename3);
9 data2 = xlsread(filename5);
10 data3 = xlsread(filename6);
11 data4 = xlsread(filename9);
12
13 ss=6;
14 figure, hold on
15 plot(data1(:,1),data1(:,2),'-r','LineWidth',2)%'MarkerFaceColor','b','MarkerSize',ss
   ).
16 plot(data2(:,1),data2(:,2),'-k','LineWidth',2)%'MarkerFaceColor','b','MarkerSize',ss
   )
17 plot(data3(:,1),data3(:,2),'-g','LineWidth',2)%'MarkerFaceColor','b','MarkerSize',ss
   )
18 plot(data4(:,1),data4(:,2),'-b','LineWidth',2)%'MarkerFaceColor','b','MarkerSize',ss
   )
19
20 legend('AU (SS = 0)', 'AU filtrate from COM (supplier)', 'AU filtrate from CaOx ([Ca
   ]=6.0mM [Ox]=1.2mM)', 'AU filtrate from CaOx ([Ca]=4.3mM [Ox]=4.3mM)')
21 xlim([380 1800])
22 ylim([5000 35*1000])
23 hXLabel = xlabel('Raman Shift (cm-1)', 'FontSize',30);%, 'FontWeight', 'bold'
24 hYLabel = ylabel('Intensity [a.u]', 'FontSize',30);%, 'FontWeight', 'bold'
25 %axesm('FontWeight', bold)
26
27 set(gca, ...
28 'FontSize',20,...
```

```
29 'FontWeight' , 'bold' , ...
30 'Box' , 'on' , ...
31 'TickDir' , 'in' , ...
32 'TickLength' , [.02 .02] , ...
33 'XMinorTick' , 'on' , ...
34 'YGrid' , 'off' , ...
35 'YMinorTick' , 'on' , ...
36 'XGrid' , 'off' , ...
37 'LineWidth' , 2 );
38
39 set(gcf, 'color', 'w');
40 hold off
```

B

PYTHON CODE FOR τ & k CALCULATION

A Python code (written using Anaconda Jupiter notebook) for curve fitting in order to obtain τ & k from a set of induction time experiment data points is as follows.

```
1 % The hashtag symbol for comments in python has been changed to percentage symbol to
   % match latex settings
2
3 % Loading packages
4 import pandas as pd
5 import os
6 import numpy as np
7 import matplotlib.pyplot as plt
8 from sklearn.metrics import r2_score
9 from scipy.optimize import curve_fit % for optimization of tau & k parameters
10 import matplotlib.gridspec as gridspec
11
12 % Load Files , change path according to your setting
13 F_path='E:\Desktop\kidney stone project\MFD\c1.2-c6.0.xlsx' % my file path
14 F = pd.read_excel(F_path)
15 F.name=os.path.basename(F_path)
16
17 % Pnucl defines the Weibull model nucleation probability
18 % Freq is the experimental nucleation probability
19
20 % Creating a function that returns the predicted Pnucl given the time(t) and the 2
   % constants (tau,k)
21 def Pnucl(t,tau,k):
22     return(1-np.exp(-((t/tau)**k))) % the formula within = Pnucl
23
24 % set initial values for optimization
25 COM_initial = [1,2] % guess values for COM
26 COD_initial = [5,0.1] % guess values for COD
27
28 % Calculating the confidence intervals for tau and k
29 import scipy
30 from math import sqrt
31 def cal_CI(parameters,covmatrix): % covmatrix = variance of optimised tau and k
   % values where parameters refer to optimised tau and k values
32     result=[]
33     for i in range(len(parameters)):
34         lower=np.round(parameters[i]-scipy.stats.norm.ppf(0.975)*sqrt(covmatrix[i][i]
   % ) ,2)
```

```

35     upper=np.round(parameters[i]+scipy.stats.norm.ppf(0.975)*sqrt(covmatrix[i][i
        ]),2)
36     tmp=np.round(parameters[i],2)
37     result.append([str(lower),str(upper)])
38     return result
39 parameters={}
40
41 % convert from COM data frame form into just an array
42 t_com = F['Time'].values
43 N_com = F['Freq (COM)'].values
44
45 % Fitting model to COM data
46 % training phase
47 c,cov = curve_fit(Pnucl,t_com,N_com,COM_initial)
48 parameters['1.2-5hrs.xlsx COM']=[c,cov,1]
49 print(F.name)
50 print(f'parameter and confidence intervals are {cal_CI(c,cov)}')
51 print(f'optimized parameters of {F.columns[1]}',c)
52 % c values defines values that reduces the error between experimental data and the
    model
53
54 % prediction phase
55 y_com_1 = np.empty(len(F['Time']))
56 for i in range(len(F['Time'])):
57     y_com_1[i] = Pnucl(F['Time'][i],*c) % make predictions using fitted function
58
59
60 % As COD values are much lower than 1 and the model is more suitable to predict
    values with larger range, hence I rescaled the original COD data during the
    training phase. The scalar=1/max(N_cod) was multiplied to original COD data. Once
    the training was over, we needed to divide the predicted values with the same
    scalar during the prediction phase.
61
62 % convert from COD data frame form into just an array
63 t_cod = F['Time'].values
64 N_cod = F['Freq (COD)'].values
65
66 scalar=1/np.max(N_cod)
67
68 % Fitting model to COD data
69 % training phase
70 c,cov = curve_fit(Pnucl,t_cod,N_cod*scalar,COD_initial)
71 parameters['1.2-5hrs.xlsx COD']=[c,cov,scalar]
72 print(F.name)
73 print(f'parameter and confidence intervals are {cal_CI(c,cov)}')
74 print(f'optimized parameters of {F.columns[2]} is {c}. Scalar is {scalar}')
75
76 % prediction phase
77 y_cod_1 = np.empty(len(F['Time']))
78 for i in range(len(F['Time'])):
79     y_cod_1[i] = Pnucl(F['Time'][i],*c)/scalar % make predictions using fitted
        function
80
81 % A function to draw confidence band
82 def confidence_band(axs,name,parameters,color,xrange=[0,300,100]):
83     c=parameters[name][0] # fitted parameter

```

```

84 cov=parameters[name][1] # fitted covmatrix
85 scalar=parameters[name][2]
86
87 upper=np.ones_like(np.linspace(*xrange))*1e-6 % upper bound of confidence band
88 lower=np.ones_like(np.linspace(*xrange))*1e6 % lower bound of confidence band
89 for i in np.linspace(*[*cal_CI(c,cov)[0],100]):
90     for j in np.linspace(*[*cal_CI(c,cov)[1],100]):
91         tmp=Pnucl(np.linspace(0,300,100), *[i,j])/scalar
92         upper=np.maximum(upper,tmp) % obtain upper bound
93         lower=np.minimum(lower,tmp) % obtain lower bound
94     axs.fill_between(np.linspace(*xrange), upper, lower,color = color, alpha = 0.5)
95     % draw confidence band
96
97 % Plotting data points with curve fitting
98
99 fig,axs=plt.subplots(3,2)
100 fig.set_size_inches(15,20)
101 fig.subplots_adjust(wspace=0.4)
102 fig.subplots_adjust(hspace=0.4)
103
104 % subplot at location [0][0]
105 axs[0][0].set_title('c1.2-c6.0 (total droplets = 55)')
106 axs[0][0].plot(F['Time'],F['Freq (COM)'],'r^',label='COM')
107 axs[0][0].plot(F['Time'],y_com_1,'k--')
108 confidence_band(axs[0][0], '1.2-5hrs.xlsx COM',parameters, 'r',xrange=[0,300,100]) %
109     draw confidence band
110 axs[0][0].plot(F['Time'],F['Freq (COD)'],'b^',label='COD')
111 axs[0][0].plot(F['Time'],y_cod_1,'k--',label='Weibull')
112 confidence_band(axs[0][0], '1.2-5hrs.xlsx COD',parameters, 'b',xrange=[0,300,100]) %
113     draw confidence band
114 axs[0][0].set_xlabel('Detection time [min]', fontsize=13)
115 axs[0][0].set_ylabel('Cumulative nucleation probability ', fontsize=13)
116 axs[0][0].legend(loc='lower right')
117 extent = axs[0][0].get_window_extent().transformed(fig.dpi_scale_trans.inverted())
118 fig.savefig('1.2mM 90 droplets.png', bbox_inches=extent.expanded(1.25, 1.26)) %
119     adjust 2 parameters

```


BIBLIOGRAPHY

- [1] I. Zahid, A. Bawazir, and R. Naser, *Plant based native therapy for the treatment of kidney stones in aurangabad (ms)*. Journal of Pharmacognosy and Phytochemistry **1** (2013).
- [2] H. Han, A. M. Segal, J. L. Seifeter, and J. T. Dwyer, *Nutritional management of kidney stones (nephrolithiasis)*, Clinical nutrition research **4**, 137 (2015).
- [3] J. W. Mullin, *Crystallization* (Elsevier, 2001).
- [4] W. P. Hartl, H. Klapper, B. Barbier, H. J. Ensikat, R. Dronskowski, P. Müller, G. Ostendorp, A. Tye, R. Bauer, and W. Barthlott, *Diversity of calcium oxalate crystals in cactaceae*, Botany **85**, 501 (2007).
- [5] J. Dalmolen, *Synthesis and Application of New Chiral Amines in Dutch Resolution*, Ph.D. thesis, PhD Thesis, University of Groningen (2005).
- [6] W. D. Callister, *Materials science and engineering an introduction* (John Wiley, 2007).
- [7] D. A. Long and D. Long, *The raman effect: a unified treatment of the theory of raman scattering by molecules*, (2002).
- [8] Nikon, <https://www.microscopyu.com/techniques/polarized-light/principles-of-birefringence>, .
- [9] T. Yu, *Kidney stones in -reactors: Design/production of microfluidic devices for induction time experiments and a comparison between laboratory and micro scale reactors*, (2019).
- [10] J. Streit, L.-C. Tran-Ho, and E. Königsberger, *Solubility of the three calcium oxalate hydrates in sodium chloride solutions and urine-like liquors*, Monatshefte für Chemie/Chemical Monthly **129**, 1225 (1998).
- [11] C. D. Scales Jr, A. C. Smith, J. M. Hanley, C. S. Saigal, U. D. in America Project, *et al.*, *Prevalence of kidney stones in the united states*, European urology **62**, 160 (2012).
- [12] T. Alelign and B. Petros, *Kidney stone disease: an update on current concepts*, Advances in urology **2018** (2018).
- [13] V. O. Edvardsson, O. S. Indridason, G. Haraldsson, O. Kjartansson, and R. Palsson, *Temporal trends in the incidence of kidney stone disease*, Kidney international **83**, 146 (2013).
- [14] G. Curhan, *Dietary calcium, dietary protein, and kidney stone formation*. Mineral and electrolyte metabolism **23**, 261 (1997).
- [15] E. N. Taylor, M. J. Stampfer, and G. C. Curhan, *Dietary factors and the risk of incident kidney stones in men: new insights after 14 years of follow-up*, Journal of the American Society of Nephrology **15**, 3225 (2004).
- [16] J. M. Teichman, *Acute renal colic from ureteral calculus*, New England Journal of Medicine **350**, 684 (2004).
- [17] B. Özokutan, M. Küçükaydin, Z. Gündüz, M. Kabaklioğlu, H. Okur, and C. Turan, *Urolithiasis in childhood*, Pediatric surgery international **16**, 60 (2000).
- [18] A. P. Evan, *Physiopathology and etiology of stone formation in the kidney and the urinary tract*, Pediatric Nephrology **25**, 831 (2010).
- [19] F. Grases, O. Söhnle, and A. Costa-Bauza, *Renal stone formation and development*, International urology and nephrology **31**, 591 (1999).
- [20] K. P. Aggarwal, S. Narula, M. Kakkar, and C. Tandon, *Nephrolithiasis: molecular mechanism of renal stone formation and the critical role played by modulators*, BioMed research international **2013** (2013).

- [21] J. Manissorn, K. Fong-ngern, P. Peerapen, and V. Thongboonkerd, *Systematic evaluation for effects of urine pH on calcium oxalate crystallization, crystal-cell adhesion and internalization into renal tubular cells*, *Scientific reports* **7**, 1 (2017).
- [22] A. Langdon and B. Grohe, *The osteopontin-controlled switching of calcium oxalate monohydrate morphologies in artificial urine provides insights into the formation of papillary kidney stones*, *Colloids and Surfaces B: Biointerfaces* **146**, 296 (2016).
- [23] C. Türk, A. Petřík, K. Sarica, C. Seitz, A. Skolarikos, M. Straub, and T. Knoll, *Eau guidelines on interventional treatment for urolithiasis*, *European urology* **69**, 475 (2016).
- [24] R. Walton, J. Kavanagh, B. Heywood, and P. Rao, *Calcium oxalates grown in human urine under different batch conditions*, *Journal of crystal growth* **284**, 517 (2005).
- [25] V. N. Ratkalkar and J. G. Kleinman, *Mechanisms of stone formation*, *Clinical reviews in bone and mineral metabolism* **9**, 187 (2011).
- [26] F. J. Opalko, J. Adair, and S. Khan, *Heterogeneous nucleation of calcium oxalate trihydrate in artificial urine by constant composition*, *Journal of crystal growth* **181**, 410 (1997).
- [27] C. F. Verkoelen, B. G. van Der Boom, and J. C. Romijn, *Identification of hyaluronan as a crystal-binding molecule at the surface of migrating and proliferating mdck cells*, *Kidney international* **58**, 1045 (2000).
- [28] N. W. Poon and M. D. I. Gohel, *Urinary glycosaminoglycans and glycoproteins in a calcium oxalate crystallization system*, *Carbohydrate research* **347**, 64 (2012).
- [29] A. Verhulst, M. Asselman, V. P. Persy, M. S. Schepers, M. F. Helbert, C. F. Verkoelen, and M. E. De Broe, *Crystal retention capacity of cells in the human nephron: involvement of cd44 and its ligands hyaluronic acid and osteopontin in the transition of a crystal binding-into a nonadherent epithelium*, *Journal of the American Society of Nephrology* **14**, 107 (2003).
- [30] M. Asselman, A. Verhulst, E. S. Van Ballegooijen, C. H. Bangma, C. F. Verkoelen, and M. E. De Broe, *Hyaluronan is apically secreted and expressed by proliferating or regenerating renal tubular cells*, *Kidney international* **68**, 71 (2005).
- [31] C. Lamontagne, G. E. Plante, and M. Grandbois, *Characterization of hyaluronic acid interaction with calcium oxalate crystals: implication of crystals faces, pH and citrate*, *Journal of Molecular Recognition* **24**, 733 (2011).
- [32] M. Asselman, A. Verhulst, M. E. de Broe, and C. F. Verkoelen, *Calcium oxalate crystal adherence to hyaluronan-, osteopontin-, and cd44-expressing injured/regenerating tubular epithelial cells in rat kidneys*, *Journal of the American Society of Nephrology* **14**, 3155 (2003).
- [33] W. Robertson and D. Scurr, *Modifiers of calcium oxalate crystallization found in urine. i. studies with a continuous crystallizer using an artificial urine*, *The Journal of urology* **135**, 1322 (1986).
- [34] M. Li, N. Blacklock, and J. Garside, *Effects of magnesium on calcium oxalate crystallization*, *The Journal of urology* **133**, 122 (1985).
- [35] D. P. Griffith, D. Musher, and C. Itin, *Urease. the primary cause of infection-induced urinary stones*, *Investigative urology* **13**, 346 (1976).
- [36] P. Arndt, N. Leistner, S. Neuss, D. Kaltbeitzel, G. Brook, and J. Grosse, *Artificial urine and fbs supplemented media in cytocompatibility assays for plga-peg-based intravesical devices using the urothelium cell line urotsa*, *Journal of Biomedical Materials Research Part B: Applied Biomaterials* **106**, 2140 (2018).
- [37] D. S. Ipe, E. Horton, and G. C. Ulett, *The basics of bacteriuria: strategies of microbes for persistence in urine*, *Frontiers in cellular and infection microbiology* **6**, 14 (2016).
- [38] S. Chutipongtanate and V. Thongboonkerd, *Systematic comparisons of artificial urine formulas for in vitro cellular study*, *Analytical biochemistry* **402**, 110 (2010).

- [39] F. Grases, A. Costa-Bauzá, E. Königsberger, and L.-C. Königsberger, *Kinetic versus thermodynamic factors in calcium renal lithiasis*, *International urology and nephrology* **32**, 19 (2000).
- [40] S. S. Atanassova and I. S. Gutzow, *Hippuric acid as a significant regulator of supersaturation in calcium oxalate lithiasis: the physiological evidence*, *BioMed research international* **2013** (2013).
- [41] W. N. A. Mazli, M. A. Ahmad, and S. Samsuri, *Nucleation*, in *Synthesis methods and Crystallization* (IntechOpen, 2019).
- [42] D. Kashchiev and G. Van Rosmalen, *Nucleation in solutions revisited*, *Crystal Research and Technology: Journal of Experimental and Industrial Crystallography* **38**, 555 (2003).
- [43] R. J. Davey, S. L. Schroeder, and J. H. ter Horst, *Nucleation of organic crystals—a molecular perspective*, *Angewandte Chemie International Edition* **52**, 2166 (2013).
- [44] D. Erdemir, A. Y. Lee, and A. S. Myerson, *Nucleation of crystals from solution: classical and two-step models*, *Accounts of chemical research* **42**, 621 (2009).
- [45] A. Myerson, *Handbook of industrial crystallization* (Butterworth-Heinemann, 2002).
- [46] I. Weissbuch, M. Lahav, and L. Leiserowitz, *Toward stereochemical control, monitoring, and understanding of crystal nucleation*, *Crystal growth & design* **3**, 125 (2003).
- [47] C. Brandel and J. H. ter Horst, *Measuring induction times and crystal nucleation rates*, *Faraday discussions* **179**, 199 (2015).
- [48] S. Toshev, A. Milchev, and S. Stoyanov, *On some probabilistic aspects of the nucleation process*, *Journal of Crystal Growth* **13**, 123 (1972).
- [49] R. P. Sear, *Quantitative studies of crystal nucleation at constant supersaturation: experimental data and models*, *CrystEngComm* **16**, 6506 (2014).
- [50] S. Jiang and J. H. ter Horst, *Crystal nucleation rates from probability distributions of induction times*, *Crystal growth & design* **11**, 256 (2011).
- [51] R. R. Jones, D. C. Hooper, L. Zhang, D. Wolverson, and V. K. Valev, *Raman techniques: fundamentals and frontiers*, *Nanoscale research letters* **14**, 1 (2019).
- [52] From, <https://www.stellarnet.us/wp-content/uploads/exp4raman.pdf>, ().
- [53] From, <https://www.horiba.com/uk/scientific/products/raman-spectroscopy/raman-academy/raman-faqs/is-raman-spectroscopy-qualitative-or-quantitative/>, ().
- [54] V. R. Kodati, G. E. Tomasi, J. L. Turumin, and A. T. Tu, *Raman spectroscopic identification of calcium-oxalate-type kidney stone*, *Applied spectroscopy* **44**, 1408 (1990).
- [55] V. Castiglione, P. Y. Sacre, E. Cavalier, P. Hubert, R. Gadisseur, and E. Ziemons, *Raman chemical imaging, a new tool in kidney stone structure analysis: Case-study and comparison to fourier transform infrared spectroscopy*, *PLoS One* **13**, e0201460 (2018).
- [56] C. Frausto-Reyes, S. Loza-Cornejo, T. Terrazas, M. de la Luz Miranda-Beltrán, X. Aparicio-Fernández, B. M. López-Macías, S. E. Morales-Martínez, and M. Ortiz-Morales, *Raman spectroscopy study of calcium oxalate extracted from cacti stems*, *Applied spectroscopy* **68**, 1260 (2014).
- [57] H. G. Edwards, M. R. Seaward, S. J. Attwood, S. J. Little, L. F. de Oliveira, and M. Tretiach, *Ft-raman spectroscopy of lichens on dolomitic rocks: an assessment of metal oxalate formation*, *Analyst* **128**, 1218 (2003).
- [58] R. Selvaraju, A. Raja, and G. Thirupathi, *Ft-raman spectral analysis of human urinary stones*, *Spectrochim Acta A Mol Biomol Spectrosc* **99**, 205 (2012).
- [59] W. Robertson, D. Scurr, and C. M. Bridge, *Factors influencing the crystallisation of calcium oxalate in urine-critique*, *Journal of Crystal Growth* **53**, 182 (1981).

- [60] C. Tornos, E. Silva, A. El-Naggar, and K. Pritzker, *Calcium oxalate crystals in breast biopsies*, *Am J Surg Pathol* **14**, 961 (1990).
- [61] P. A. Isotalo and R. V. Lloyd, *Presence of birefringent crystals is useful in distinguishing thyroid from parathyroid gland tissues*, *The American journal of surgical pathology* **26**, 813 (2002).
- [62] A. Luqman, J. Stanifer, O. M. A. Siddiqui, A. Naseer, and B. M. Wall, *Calcium oxalate monohydrate crystals: a clue to ethylene glycol poisoning*, *The American journal of the medical sciences* **341**, 338 (2011).
- [63] P. Brown, D. Ackermann, and B. Finlayson, *Calcium oxalate dihydrate (weddellite) precipitation*, *Journal of crystal growth* **98**, 285 (1989).
- [64] From, <https://www.mindat.org/min-4254.html>, .
- [65] R. E. Stoiber and S. A. Morse, *Biaxial crystal optics*, in *Crystal Identification with the Polarizing Microscope* (Springer US, Boston, MA, 1994) pp. 159–171.
- [66] D. Griffith, https://vapaa.wildapricot.org/resources/documents/va_stones-keypoints.pdf, .
- [67] C. N. Baroud, F. Gallaire, and R. Dangla, *Dynamics of microfluidic droplets*, *Lab on a Chip* **10**, 2032 (2010).
- [68] J. Ferreira, F. Castro, F. Rocha, and S. Kuhn, *Protein crystallization in a droplet-based microfluidic device: Hydrodynamic analysis and study of the phase behaviour*, *Chemical Engineering Science* **191**, 232 (2018).
- [69] L. Li and R. F. Ismagilov, *Protein crystallization using microfluidic technologies based on valves, droplets, and slipchip*, (2010).
- [70] B. R. Benson, H. A. Stone, and R. K. Prud'homme, *An “off-the-shelf” capillary microfluidic device that enables tuning of the droplet breakup regime at constant flow rates*, *Lab on a Chip* **13**, 4507 (2013).
- [71] C. Holtze, *Large-scale droplet production in microfluidic devices—an industrial perspective*, *Journal of Physics D: Applied Physics* **46**, 114008 (2013).